Journal Pre-proof



Cryogenic microcrack mitigation and hydrogen permeability in a carbon fibre composite with a hybrid epoxy matrix

James C. Griffith, Siyang Wang, Christopher P. Jones, Lui Skytree, Ricky Mazzeo, Cameron G. Woodgate, Huw Edwards, Karthik R. Ramakrishnan, Sébastien Rochat, Finn Giuliani, Marcus Walls-Bruck, Ian Hamerton

PII: S1359-8368(26)00880-2

DOI: https://doi.org/10.1016/j.compositesb.2026.114259

Reference: JCOMB 114259

To appear in: *Composites Part B*

Received Date: 1 July 2026

Revised Date: 26 August 2026

Accepted Date: 30 September 2026

Please cite this article as: Griffith JC, Wang S, Jones CP, Skytree L, Mazzeo R, Woodgate CG, Edwards H, Ramakrishnan KR, Rochat S, Giuliani F, Walls-Bruck M, Hamerton I, Cryogenic microcrack mitigation and hydrogen permeability in a carbon fibre composite with a hybrid epoxy matrix, *Composites Part B*, https://doi.org/10.1016/j.compositesb.2026.114259.

This is a PDF of an article that has undergone enhancements after acceptance, such as the addition of a cover page and metadata, and formatting for readability. This version will undergo additional copyediting, typesetting and review before it is published in its final form. As such, this version is no longer the Accepted Manuscript, but it is not yet the definitive Version of Record; we are providing this early version to give early visibility of the article. Please note that Elsevier's sharing policy for the Published Journal Article applies to this version, see: https://www.elsevier.com/about/policies-and-standards/sharing#4-published-journal-article. Please also note that, during the production process, errors may be discovered which could affect the content, and all legal disclaimers that apply to the journal pertain.

© 2026 Published by Elsevier Ltd.

Journal Pre-proof

Cryogenic microcrack mitigation and hydrogen permeability in a carbon fibre composite with a hybrid epoxy matrix

James C. Griffith[1], Siyang Wang[2], Christopher P. Jones[3], Lui Skytree[1], Ricky Mazzeo[1], Cameron G. Woodgate[4], Huw Edwards[1,5], Karthik R. Ramakrishnan[1,5], Sébastien Rochat[1,6], Finn Giuliani[2], Marcus Walls-Bruck[5], Ian Hamerton[1,5]

[1] Bristol Composites Institute, School of Civil, Aerospace, and Design Engineering, University of Bristol, Queen's Building, University Walk, Bristol, BS8 1TR, UK.

[2] Department of Materials, Imperial College London, Prince Consort Road, London, SW7 2BP, UK.

[3] Interface Analysis Centre, HH Wills Physics Laboratory, University of Bristol, Tyndall Avenue, Bristol, BS8 1TL, UK.

[4] Department of Chemistry, Imperial College London, White City Campus, London, W12 0BZ, UK.

[5] NCC, Bristol and Bath Science Park, Feynman Way Central, Emersons Green, Bristol BS16 7FS, UK.

[6] School of Engineering Mathematics and Technology, Ada Lovelace Building, Tankard's Close, Bristol, BS8 1TW, UK.

Corresponding author email: James.Griffith@bristol.ac.uk

Keywords: Carbon fibre composites; Cryogenic microcracking; Hydrogen permeability; Cryo-scanning electron microscopy.

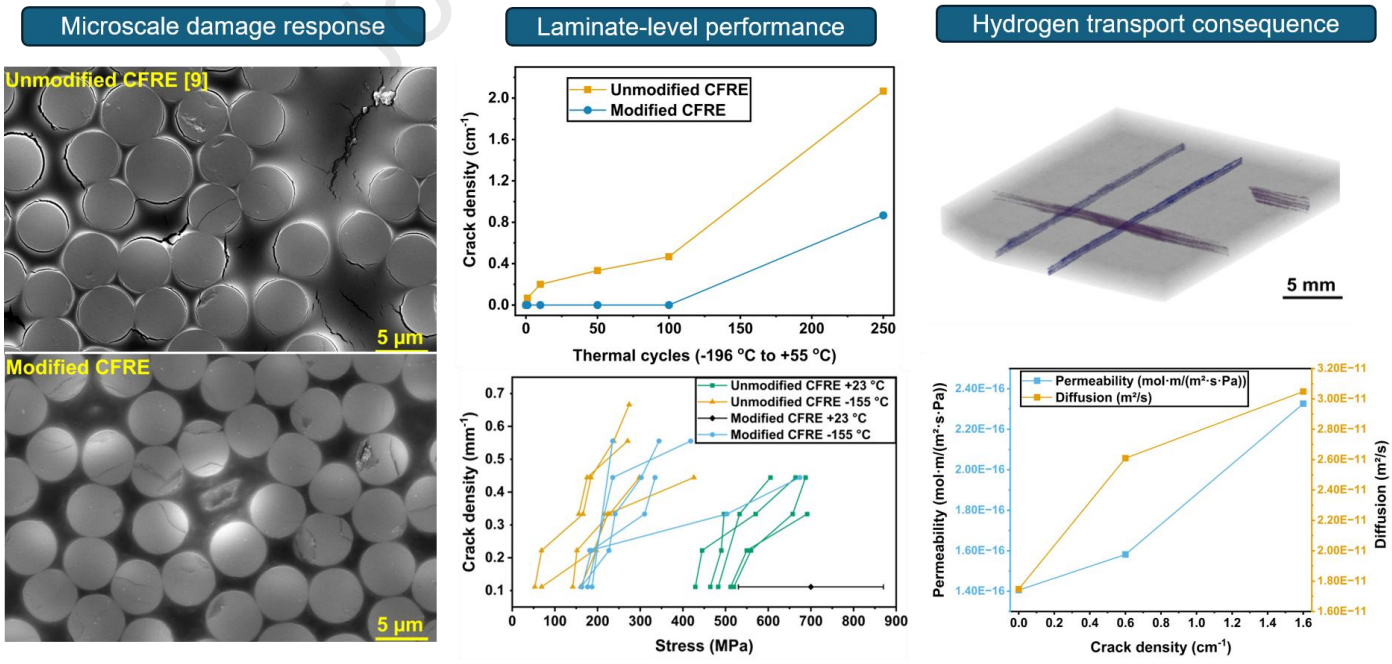
Abstract

Carbon fibre reinforced polymer (CFRP) tanks are attractive for liquid hydrogen (LH_2) storage, but cryogenic matrix microcracking can increase gas permeability and compromise reliability. This work investigates an epoxy matrix modified with core–shell rubber (CSR), nanosilica and

Journal Pre-proof

polysulphide in carbon fibre reinforced epoxy (CFRE) laminates, providing a multiscale assessment linking cryogenic microcrack resistance and hydrogen permeability with *in-situ* observation of microscale damage mechanisms. The modified CFRE showed no transverse cracking up to 100 cycles and a 58% lower crack density than the unmodified system after 250 cycles between −196 °C and +55 °C. Preliminary hydrogen (H_2) permeation data suggested that, after 250 cycles, microcracking increased permeability mainly through higher diffusivity rather than leakage, with X-ray computed tomography (xCT) showing no through-thickness interconnected crack network. Cryogenic scanning electron microscopy (cryo-SEM) showed no microscale matrix cracking or fibre–matrix debonding under rapid thermal shock or gradual cooling. Additional focussed ion beam–scanning electron microscopy (FIB-SEM) analysis provided evidence that isolated fibre damage can extend into the fibre interior. Under combined thermo-mechanical loading at −155 °C, the minimum measured stress at first crack was 204% higher in the modified CFRE. Overall, cryogenic microcracking mitigation in the modified CFRE depends on suppressing thermally induced microscale damage initiation, rather than on cryogenic matrix toughness or coefficient of thermal expansion (CTE) mismatch alone.

Graphical abstract



Journal Pre-proof

1. Introduction

Carbon fibre–reinforced polymers (CFRP) are widely used in aerospace and other weight-critical structures due to their low density, high specific strength and stiffness, and the ability to tailor properties through laminate design and anisotropy. These attributes have driven increasing interest in CFRPs for cryogenic propellant storage, particularly for liquid hydrogen (LH_2) in zero carbon-emission aircraft, as well as in ground-based transport and storage applications [1, 2]. Although storage pressures are lower than in compressed hydrogen systems, LH_2 introduces an extremely low-temperature environment (−253 °C) that places significant demands on the storage material. Traditionally, metallic tanks have been used, particularly in space applications; however, metals can suffer from hydrogen embrittlement and associated performance limitations [3]. CFRP tanks, by contrast, offer a potential weight saving of around 20–40% compared with metallic tanks, although their performance is instead limited by thermally induced damage and hydrogen permeability, both of which must be controlled for reliable and safe operation [4, 5].

Transverse matrix microcracking is one of the primary damage mechanisms experienced by CFRPs in cryogenic environments, thought to be driven by thermally induced residual stresses arising from thermal expansion mismatch at both the constituent and ply-level scales [6]. At the constituent level, the mismatch is significant, with epoxy matrices typically having CTEs of ~50 μm/(m·°C), while carbon fibres have a longitudinal CTE of ~ −1 μm/(m·°C) and a macroscopic transverse CTE of ~ 8 μm/(m·°C) [7, 8]. To better understand cryogenic damage mechanisms that result from this anisotropic thermal response, a range of *in-situ* characterisation techniques have been recently developed and used [9-17]. These include cryogenic *in-situ* optical microscopy with video capture of microcrack formation under tensile loading using a 3D-printed cryostat with a viewing port [9-11], and cryogenic tensile testing combined with *in-situ* optical microscopy on cross-ply thin-ply CFRP laminates using a Gifford–McMahon cryocooler [12]. Acoustic emission monitoring has also been employed, including fibre-optic sensor-based systems for *in-situ* damage detection in woven CFRP under cryogenic conditions, as reported by Su *et al.* [13, 14] and Ma *et al.* [15]. In addition, cryogenic *in-situ* micro-computed

Journal Pre-proof

tomography (μCT) tensile testing has been used for three-dimensional damage assessment in both quasi-isotropic CFRP laminates and glass/epoxy woven fabric composites, as reported by Li *et al.* [16, 17]. While these methods enable *in-situ* visualisation or monitoring of damage development, cryo-scanning electron microscopy (cryo-SEM) has more recently been shown to directly resolve damage at the fibre–matrix scale [9]. This included continuous, high-resolution visualisation of fibre–matrix interfacial debonding, matrix cracking, and fibre cracking on cooling in a CFRP with a commercial, untoughened epoxy matrix. This combination of mesoscale and microscale damage characterisation provides a basis for the present study, which examines damage formation in a modified epoxy matrix for cryogenic applications.

A major barrier to the adoption of CFRP for cryogenic storage is the increase in gas permeability caused by thermally induced damage, a challenge highlighted early during preflight proof testing of the Lockheed-Martin X-33 vehicle, where failure of the sandwich CFRP LH_2 tank was linked to cryogenic microcracking of the inner skin and subsequent hydrogen infiltration into the core [18]. Since then, numerous studies have examined how cryogenic thermal fatigue affects gas transport in fibre-reinforced polymers [19-24]. Bechel *et al.* showed that lay-up and thermal-cycle hold temperatures strongly influence crack initiation, propagation and the formation of through-thickness gas-flow paths [19]. Choi and Sankar reported that cryogenic cycling increased gas permeability in graphite/epoxy laminates, while textile composites remained less permeable than laminated composites after cycling [20]. Flanagan *et al.* investigated CF/PEEK laminates for cryogenic tanks and showed that permeability was affected by cryogenic cycling, manufacturing route, constituent materials, pressure and laminate thickness [21]. Saha *et al.* reported that stitching can increase permeability in 3D stitched carbon/epoxy composites through cracking in resin-rich seam regions, with microcrack density increasing with thermal cycling, while their later thin-ply study showed that incorporating thin plies into stitched laminates suppressed cryogenic microcracking and reduced gas permeation [22, 23]. More recently, Koord *et al.* reported that, for IM7/8552 laminates cycled up to 10 times in liquid nitrogen (LN_2), microcrack density increased on cycling, while helium permeation remained unchanged [24]. The great majority of studies linking purely cryogenic cycling and microcracking to gas permeation use helium as the permeant gas [19-24], largely for reasons of

Journal Pre-proof

convenience and safety, since hydrogen is flammable above 4 vol% in air and detonable above 18.3 vol% [18, 25].

For LH_2 storage applications, however, helium remains a proxy for the gas of interest. Hydrogen leakage and permeation have been measured in mechanically damaged, loaded or tank-derived composite materials [18, 26, 27], but hydrogen transport after cryogenic thermal cycling alone is less widely reported, particularly for matrix-modified CFRP. This is important because studies have shown helium and hydrogen do not necessarily give the same transport response. When investigating helium and hydrogen leakage through X-33 tank test panels, Rivers *et al.* found that the two leak rates did not correlate [18]. Schultheiß observed that, across a range of CFRP, lined CFRP and PVC systems, helium permeability was higher than hydrogen permeability in all but one material, by 0.7-28 times, and helium diffusivity was 3.3-5.8 times higher [25]. Similarly, Humpenöder reported that helium diffusivity exceeded hydrogen diffusivity by 2.4-3.1 times, whereas permeability differences were smaller and material-dependent, with hydrogen permeability slightly exceeding helium in most of the fibre-reinforced and polymer systems examined [28]. In addition, Koord *et al.* reported helium permeability to be 3.1 times higher than hydrogen in HDPE [24]. These differences motivate the present study, in which hydrogen rather than helium was used for permeation measurements in the modified CFRE.

Given the link between cryogenically induced matrix cracking and subsequent gas permeation, matrix modification to improve microcrack resistance has been widely investigated for CFRPs intended for cryogenic storage applications [29-37]. Islam *et al.* employed polydopamine (PDA)-coated nanoparticles with low or negative thermal expansion, namely nano-cupric oxide and zirconium tungstate [29, 30]. In both cases, after a single 45 min immersion in liquid nitrogen, CFRP laminates containing the coated nanoparticles showed suppressed microcracking, whereas laminates containing the uncoated nanoparticles exhibited cracking. Wang *et al.* used the same 45 min cryogenic immersion on their block copolymer (BCP) modified epoxies to demonstrate the improved resistance to microcracking at an optimal loading of 2.5 wt% BCP in CFRP laminates [31]. Qu *et al.* toughened an epoxy matrix using two hydroxyl-terminated polyurethanes. After 200 cycles between −196 °C and room temperature,

Journal Pre-proof

the resulting CFRPs showed 15.9% and 7.1% lower microcrack densities than the untoughened CFRP, although all materials cracked early in the cycling regime [32]. He *et al.* modified an epoxy matrix with graphene oxide (GO) and Fe_3O_4/GO in one study [33], and three thermoplastics (polyether imide, polycarbonate, and polybutylene terephthalate) in another [34]. In both studies, after five cycles between −196 °C and room temperature, all modified CFRE laminates showed reduced crack densities compared to the unmodified system. In earlier studies, Nobelen *et al.* reported that increasing additions of carboxyl-terminated butadiene acrylonitrile (CTBN) liquid rubber reduced, and in some cases eliminated, microcracking over five cycles [35], while dispersed CSR particles reduced microcrack density by ~50% after five cycles [36]. Timmerman *et al.* also found that nanoclay addition reduced microcracking by ~50% compared to the unmodified control laminate, although higher nanoclay loadings led to increased microcracking [37].

Despite substantial work on cryogenic damage characterisation, hydrogen permeation and matrix modification in CFRP, their combined investigation in a modified CFRE system has not, to the authors' knowledge, been reported. The present study addresses this gap through a multiscale assessment of the modified CFRE, linking laminate-scale crack mitigation, hydrogen transport behaviour, xCT-resolved internal cracking and in-situ microscale damage observations to explain how the matrix modification suppresses cryogenic damage initiation. The study begins by assessing the resistance of the modified CFRE to thermally induced matrix microcracking during repeated thermal cycling between −196 °C and +55 °C. The effect of microcracking on hydrogen permeability is then examined directly, with xCT used to assess internal cracking and whether a through-thickness interconnected crack network formed within the permeation-tested specimens. To understand the underlying damage mechanisms, cryo-SEM is used to visualise in-situ microscale damage formation in the modified CFRE under both controlled cooling and thermal shock conditions. A separate FIB-SEM analysis is used to assess whether localised fibre damage following cryogenic exposure can extend into the fibre interior. Temperature-dependent fracture testing of the matrix is then used to provide matrix-level context for the observed laminate and microscale behaviour. Finally, the implications of the matrix modification under combined cryogenic and mechanical loading are assessed through

Journal Pre-proof

determination of the tensile stress at first crack, allowing the results to be considered in the context of LH_2 storage tanks. Throughout the study, several references are made to methods, data and images first reported in our previous work characterising the unmodified CFRE under cryogenic conditions [9]. These are reproduced or adapted here for comparison with the modified CFRE.

2. Materials and methods

2.1. Materials

RS-M135 (PRF Composites, Poole, UK) was used as the epoxy matrix. The formulation is based on the diglycidyl ether of bisphenol A (DGEBA; CAS No. 1675-54-3, 75–90 wt%) with 1,6-hexanediol (CAS No. 933999-84-9, 10–20 wt%) and has an epoxy equivalent weight (EEW) of 176 g/eq. The core-shell rubber toughener used was Kane Ace MX-150 (Kaneka, Belgium), which contains a polybutadiene rubber (PBR) core as a pre-dispersed masterbatch (40 wt% in DGEBA) (EEW = 307 g/eq) with 100 nm and 200 nm particles. The nanosilica modifier used was Nanopox F400 (Evonik, Germany), supplied as a pre-dispersed masterbatch (40 wt% in DGEBA) (EEW = 314 g/eq). The epoxy-terminated polysulphide modifier used was Thioplast EPS35 (Nouryon, Sweden) (EEW = 625 g/eq). The amine curing agent used was RS-MH137 (PRF Composites, Poole, UK), containing poly(oxypropylene) diamine (CAS No. 9046-10-0) (50-75 wt%) (AEW = 52 g/eq) and 3-aminomethyl-3,5,5-trimethylcyclohexylamine (CAS No. 2855-13-2) (25-50 wt%). The modified matrix formulation was selected from a wider matrix-development study reported separately [38]. HexTow IMA-GP 12 K fibres (Hexcel Reinforcements, Dagneux, France) were used as the unidirectional carbon fibre reinforcement.

2.2. Manufacturing and specimen preparation

Unmodified epoxy specimens for fracture testing and thermomechanical analysis were prepared by mixing RS-M135 and RS-MH137 in a ratio of 100:30 by weight. Modified epoxy specimens were prepared by mixing RS-M135, EPS35, MX-150, and F400 in a ratio of

Journal Pre-proof

40:10:25:25 by weight at 60 °C to achieve a 10 wt% concentration of each modifier. A stoichiometric amount (a ratio of 100:21 by weight) of the RS-MH137 hardener was added based on the calculated EEW of the blend. The blends were degassed for 10 minutes before an initial room temperature cure for 24 hours was followed by a post-cure at 70 °C for 20 hours in silicone moulds with dimensions tailored to each characterisation method.

Unmodified CFRE laminates were manufactured by double bag vacuum-assisted resin transfer moulding (VARTM), as first reported in [9]. This manufacturing method was chosen to minimise the level of voids in the laminate because higher void fractions have been observed to significantly influence microcrack density during cryogenic cycling [39] and act as initiation sites for microcracks on cycling, increasing the gas leak rate of CFRPs [40]. In the current study, the modified CFRE laminates were laid up in the same manner, with an 8-ply $[0_2/90_2]_s$ stacking sequence, and the dry fibre stack left under vacuum for 24 hours at 40 °C to allow consolidation and moisture removal. This lay-up facilitated the tensile stress at first crack measurements described in Section 2.3.7, as transverse matrix microcracking in 90° plies is typically the earliest damage mode under axial loading in the 0° direction [41]. The lay-up also represents a severe configuration for thermal cycling, as the 0°/90° ply mismatch promotes laminate-level residual stresses during cooling and therefore increases susceptibility to transverse microcracking [6]. The resin system was subsequently weighed, mixed and degassed prior to infusion under vacuum at 40 °C. While the unmodified epoxy (RS-M135) could be readily infused at room temperature, the modified epoxy had a higher viscosity. Therefore, a 40 °C processing temperature was selected after dynamic and isothermal rheology was performed (Supplementary Figures S1a and b), to achieve sufficiently low viscosity (0.47 Pa·s) for effective fibre wet-out, whilst still maintaining a sufficient pot life (23 minutes) and infusion working time (20 minutes), according to the suggested upper limit of 0.8 Pa·s by Wadsworth [42]. Following infusion, the laminate was cured at room temperature for 24 hours and then post-cured at 70 °C for 20 hours. CFRE specimens were extracted and prepared for thermal cycling and H_2 permeation (25 mm × 25 mm), tensile stress at first crack testing (205 mm × 13 mm), and cryo-SEM analysis (3 mm × 5 mm), following the procedures described previously [9] and illustrated in Figure 1. The thickness of the specimens varied from 2.40 mm to 2.47 mm.

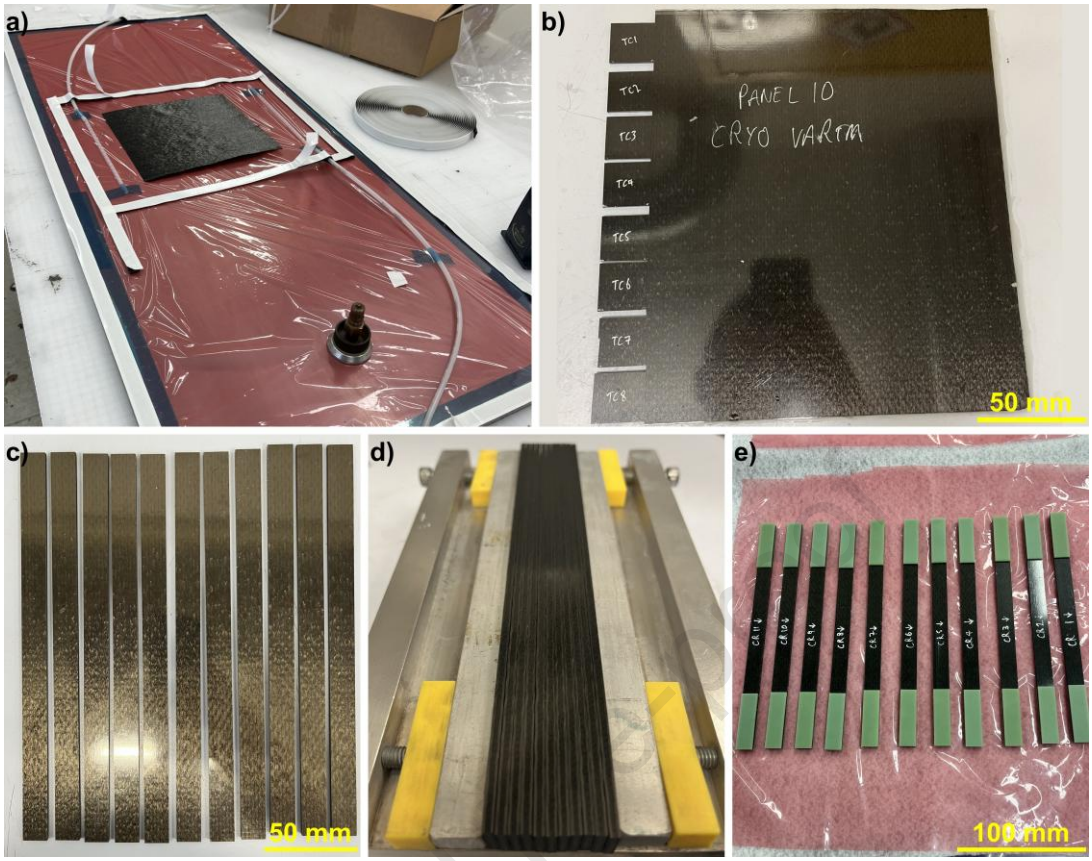


Figure 1: CFRE specimen manufacturing and preparation: a) VARTM layup; b) thermal cycling specimen extraction; c) tensile stress at first crack specimen extraction, d) polishing and e) tabbing.

2.3. Materials characterisation

2.3.1. Rheology and thermomechanical analysis

Dynamic and isothermal rheology was performed using a TA Instruments Discovery HR-10 rheometer and 25 mm ETC aluminium disposable parallel plates. Dynamic temperature sweeps were conducted from 25 °C to 140 °C at a heating rate of 2 °C min^{-1}. Thermomechanical analysis (TMA) was used to characterise thermal expansion behaviour *via* a TA Instruments Q400 fitted with an expansion probe. Calibration of temperature and dimensional response was performed using indium and aluminium standards, respectively. Specimens were cured into cubes (8 mm × 8 mm × 8 mm) and tested from -75 °C to 20 °C at a heating rate of 5 °C min^{-1}. Mean coefficients of thermal expansion (α_m) were calculated from the total measured length change (ΔL) across the full temperature range (ΔT) using Equation (1),

Journal Pre-proof

where L_0 is the initial gauge length which was measured by the instrument prior to data acquisition.

$$\alpha_m = \frac{1}{L_0}\frac{\Delta L}{\Delta T} \quad \ldots(1)$$

2.3.2. Thermal cycling

Thermal cycling was carried out according to the method first reported in [9]. In brief, three specimens were thermally cycled between −196 °C and +55 °C using an automated immersion rig with LN_2 and a heating chamber. Cycle timing was calibrated by embedded thermocouple measurements, and a 490 s cycle including 60 s LN_2 immersion was applied for 250 cycles. Optical micrographs using a Zeiss Inverted Axio Observer were collected from two adjacent polished edges of each specimen at 0, 1, 10, 50, 100 and 250 cycles to assess thermally induced microcracking.

2.3.3. Hydrogen permeability

Room temperature hydrogen permeation was characterised using a static differential-pressure method. The experimental methodology followed BS ISO 15105-1:2007 Plastics — Film and sheeting — Determination of gas-transmission rate — Part 1: Differential-pressure methods [43], in which a constant gas pressure was applied upstream of the specimen while the downstream side was held under static vacuum. Permeation was quantified by monitoring the rate of pressure rise in the downstream volume under controlled temperature and fixed volume conditions. The system comprised a gas and vacuum manifold equipped with capacitance manometers, vacuum transducers, thermocouples, and a turbomolecular pump, connected to a custom-designed permeation cell (Figure 2). The cell consisted of a pressurised upstream chamber and two evacuated chambers (downstream and side chambers), separated by the mounted specimen and deformable indium seals. The downstream chamber measured through-thickness hydrogen flux, while the side chamber was used to assess seal integrity and detect

any lateral gas leakage before and during testing. Each chamber was independently instrumented with pressure sensors and relief valves.

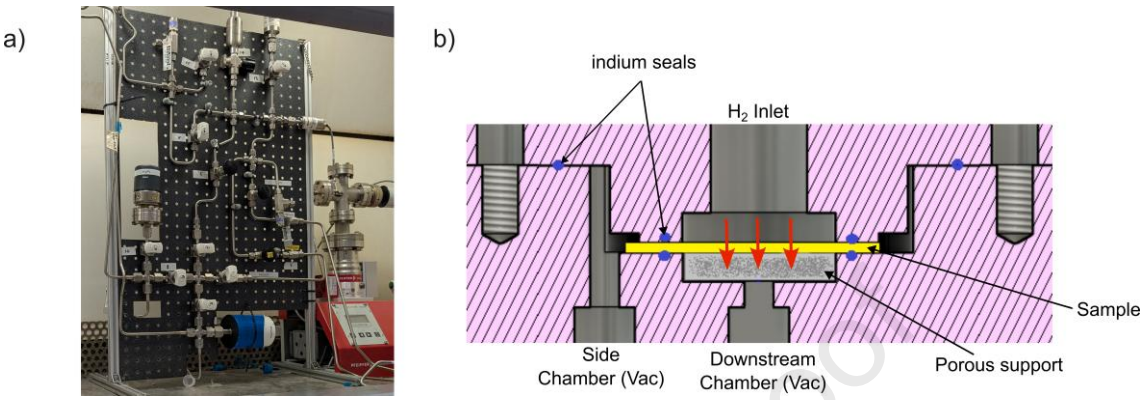


Figure 2: a) Hydrogen permeation apparatus and b) Representative cross-sectional schematic of the permeation cell assembly showing the mounted specimen (yellow) and indium seals (blue).

Hydrogen permeation measurements were carried out on as-manufactured specimens and specimens subjected to 250 thermal cycles, as described in Section 2.3.2. Prior to testing, each specimen was installed in the permeation cell body and compressed between indium wire seals, thereby isolating the upstream, downstream, and side chambers. Although each specimen measured 25 mm × 25 mm, the effective permeation area was smaller due to the permeation cell geometry and the presence of the indium wire seal. The active area was determined from pixel measurements of the nominal 19 mm diameter indium seating indent from the permeation cell and the further reduction caused by indium overlap on the specimen surface. The permeation region was assumed to remain circular, acknowledging the indium residue after removal from the permeation cell. This yielded the reduced permeation areas as reported in Table 1. The assembled cell was connected to the manifold and placed in an environmental chamber. To degas the permeation cell and sample, a 24 h dynamic vacuum was applied using a turbomolecular pump, with the cell heated to 40 °C to assist outgassing. Target pressures of ≤ 1×10^{-3} mbar in the upstream chamber and ≤ 1×10^{-5} mbar in the downstream and side chambers were achieved before cooling to ~22 °C. Each chamber was then isolated, and vacuum-decay tests were performed; assemblies exhibiting leak rates greater than 1×10^{-5}

mbar s^{-1} were dismantled and reassembled. Baseline downstream leak rates were typically ~1 × 10^{-8} mbar L s^{-1} and were recorded for background correction.

Following sample installation validation, the downstream and side chambers were re-evacuated (< 1 × 10^{-3} mbar), isolated, and allowed to stabilise. The upstream chamber was initially pressurised with hydrogen to 2 bar and monitored for 1 h to confirm the absence of positive-pressure leaks, before being increased incrementally to 50 bar. Pressures in all chambers were logged at 30 s intervals. Testing proceeded until steady-state permeation was reached, identified by a linear increase in downstream pressure. Permeability, diffusivity, and solubility coefficients were then determined using the time-lag method. The hydrogen permeability coefficient, P (mol H_2·m / (m^2·s·Pa)), was calculated from the steady-state pressure rise rate (dp/dt) using Equation (2), where dp/dt represents the steady-state rate of pressure rise in the downstream chamber, V is the downstream volume, d is the specimen thickness, A is the effective permeation area, T is the test temperature, R is the universal gas constant and p_u is the applied upstream pressure.

$$P = \frac{Vd}{ARTp_u}\left(\frac{dp}{dt}\right) \quad \ldots(2)$$

The diffusion coefficient, D (m^2/s), was obtained using the time-lag approach, in which the extrapolated x-intercept of the linear steady-state pressure time response defines the time lag, t′, which is related to D through Equation (3).

$$D = \frac{d^2}{6t'} \quad \ldots(3)$$

The solubility coefficient, S (mol/(m^3·Pa)), was then calculated by Equation (4).

$$S = \frac{P}{D} \quad \ldots(4)$$

2.3.4. X-ray computed tomography

X-ray computed tomography (xCT) was performed on specimens approximately 25 mm x 25 mm x 2.4 mm in size using a Zeiss XRadia Versa 520 system. Scans were acquired at 80 kV, 7 W with no filtering and with an exposure time of 3 s per projection during rotation of the specimen. The detector was operated with an optical magnification of 0.398x, resulting in an effective voxel size of 14.5 µm. xCT 3D reconstruction and segmentation were performed using Dragonfly 3D World (Object Research Systems (ORS) Inc., Montreal, Canada).

2.3.5. Cryogenic, ambient and focussed ion beam-scanning electron microscopy

Rapid cooling cryo-SEM imaging was performed using a FEI Quanta 200F FEG-SEM equipped with a Gatan Alto 2500 cryo-preparation system. Secondary electron images were acquired at 20 kV. Samples were mounted on a cryo-transfer holder, sputter-coated with ~10 nm Au–Pd, immersed in slush nitrogen (SN_2, ~−207 °C) for 60 s, and returned to the preparation chamber to sublime surface ice at −95 °C for 3 minutes. Specimens were then transferred directly to a pre-cooled SEM chamber and imaged at −130 °C. Slow-cooling cryo-SEM imaging was conducted using a Quanta 650 FEG-SEM (FEI UK Ltd., Cambridge, UK) fitted with a Gatan C1003 nitrogen cooling stage (Gatan Inc., CA, USA). Specimens were cooled with nitrogen gas at ~6 °C min^{-1} to −138 °C, held for approximately 9 minutes then warmed at ~2 °C min^{-1}. Secondary electron images were acquired at 20 kV after sputter-coating with gold (~10 nm), with 721 images collected at six frames per minute.

FIB-SEM was conducted on a ThermoFisher Scientific Helios 5 Hydra CX Plasma FIB microscope equipped with an Elstar Electron SEM column with UC+ and a multi-ion species plasma FIB column oriented at 52° relative to the SEM column. The specimen was positioned at a working distance of 4.1 mm, and the stage tilted to 52° so that the specimen surface was normal to the ion beam during milling. A thin platinum protective layer was deposited over the region of interest prior to milling to minimise surface damage. Fiducial markers were milled adjacent to the target region to enable alignment correction during automated slice-and-view

acquisition. Serial sectioning was performed using an argon ion beam with accelerating voltage of 30 kV and a beam current of 1 nA, with a nominal slice thickness of 25 nm. SEM images of the exposed cross-section were acquired for every slice using an accelerating voltage of 15 kV. SEM images of single-edge notched beam fracture surfaces were collected on the same instrument at 20 kV.

2.3.6. Matrix fracture toughness

Fracture toughness (K_{IC}) and fracture energy (G_{IC}) were measured by single-edge notched beam (SENB) testing at room and cryogenic temperatures. Specimens were cured to the geometries shown in Supplementary Figure S2, with W = 2B. Notches and sharp pre-cracks were introduced using a fresh razor blade, with crack lengths satisfying 0.45 < a/W < 0.55 and verified post-test by optical microscopy (Keyence VHX-6000f). Crack-tip stress relaxation was achieved by heating at 70 °C for 30 minutes prior to testing. Fracture tests were conducted on an Instron 3366 (10 kN load cell) at 10 mm min^{-1}. For −196 °C tests, specimens were immersed in liquid nitrogen for 10 minutes before loading. At least three specimens were tested per condition. Force-displacement data were analysed in accordance with ASTM D5045 [44] to determine K_{IC} using either P_{max} or P_q (Equation (5)), with test validity assessed using Equation (6), where σ_y = 0.7 times the compressive yield stress.

$$K_{IC} = \frac{P_{\max or\ q}\, f(x)}{BW^{1/2}} \quad \ldots(5)$$

$$B, a, (W - a) > 2.5\ (K_q / \sigma_y) \quad \ldots(6)$$

Fracture energy (G_{IC}) was calculated using Equations (7) and (8) from the calibration factor (φ) and corrected energy (U), where U is the difference between the integrated load–displacement area to P_{max} for the notched specimen (U_q) and that of an unnotched correction specimen (U_i) at the same temperature.

$$G_{IC} = \frac{U}{(BW\varphi)} \quad \ldots(7)$$

$$U = U_q - U_i \quad \ldots(8)$$

Journal Pre-proof

2.3.7. Tensile stress at first crack

Room temperature and cryogenic temperature quasi-static tensile testing to measure the tensile stress at first crack was performed on an Instron 5980 series universal testing system equipped with a 250 kN load cell, using the method first discussed in [10, 11] and then subsequently described in [9]. In brief, at room temperature, specimens were loaded with the polished edge facing a camera for *in-situ* microcrack observation *via* continuous video recording. For cryogenic tests, specimens with attached thermocouples were mounted in a 3D-printed cryostat and cooled with nitrogen gas to −155 °C ± 5 °C, held for 5 minutes, before tensile loading was applied at 2 mm min^{-1} with continuous video recording. Five specimens were tested at each temperature. Transverse cracks were identified visually from video recordings and matched to their initiation stress using Imetrum software. Crack density (D) was calculated over a 9 mm observation length (A) using Equation (9), where *N* is the number of visible cracks.

$$D = N / A \quad ...(9)$$

3. Results and discussion

3.1. Thermal cycling and transverse microcracking

To assess the capacity of the modified CFRE to resist thermally induced matrix cracking, three 25 mm x 25 mm specimens were subjected to 250 cycles between −196 °C and +55 °C with optical microscopy imaging at 0, 1, 10, 50, 100, and 250 cycles. For each specimen, two adjacent polished edges were inspected, with Figure 3 presenting the images from both edges of one specimen (TC_3) at 0, 100, and 250 cycles.

Journal Pre-proof

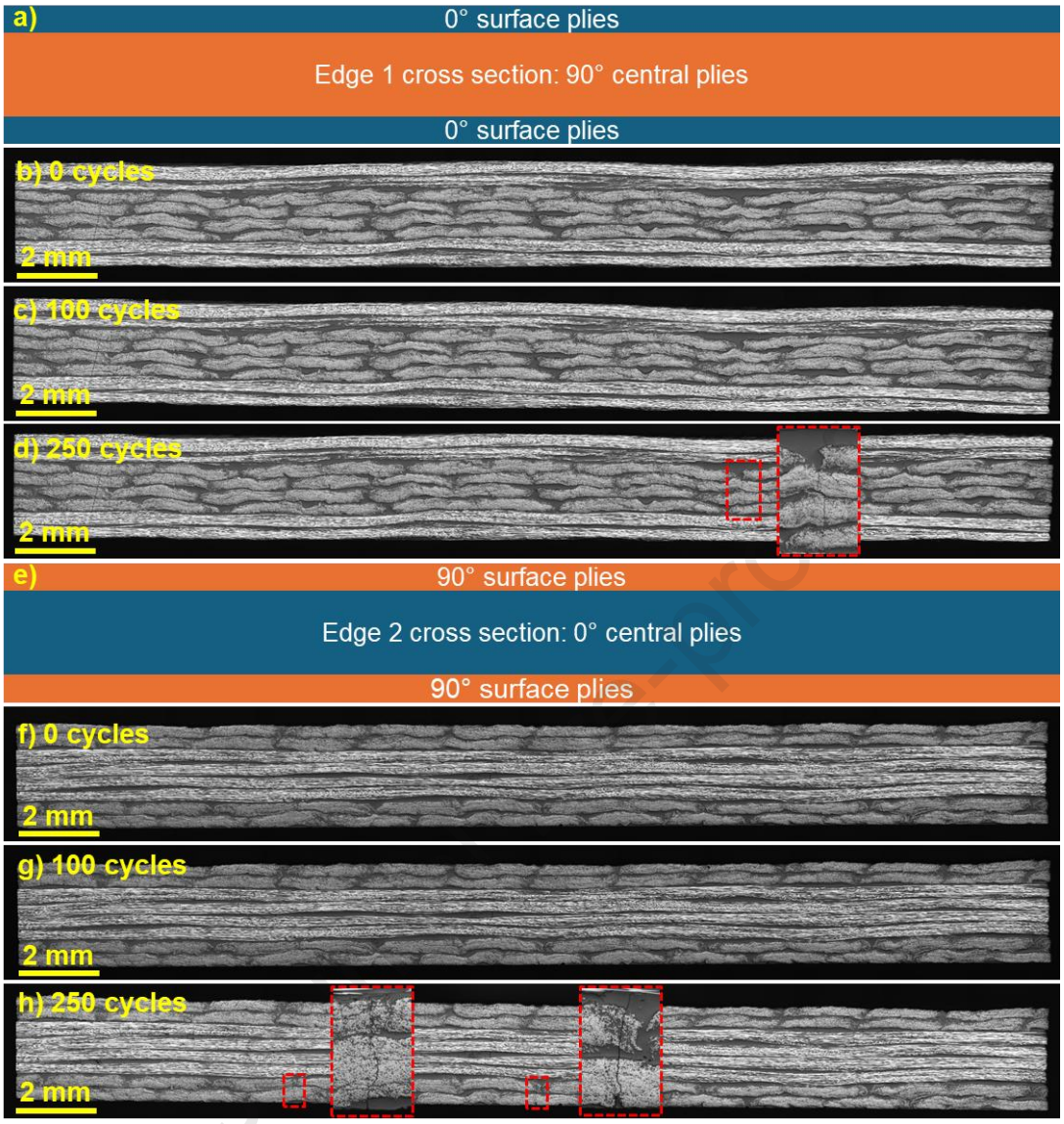


Figure 3: Microcrack evolution in the modified CFRE specimen subjected to thermal cycling between −196 °C and +55 °C: a), e) Schematics indicating the observed edges, where a) corresponds to edge 1 and e) to edge 2; b), f) prior to cycling; c), g) after 100 cycles, with no cracks observed; and d), h) after 250 cycles, showing one crack on edge 1 and two cracks on edge 2.

After 250 cycles, the observed transverse microcracks depended on the orientation of the inspected face. The laminate stacking sequence was $[0_2/90_2]_s$, comprising two 0° outer plies and four blocked 90° inner plies. Depending on the inspected edge, different ply orientations were exposed at the surface. In edge 1 (Figure 3a), the central 90° block was visible through the specimen thickness with 0° plies at the outer surfaces. In edge 2 (Figure 3e), the perpendicular cross-section exposed the 90° plies at the specimen surfaces and the 0° plies in the interior. Average microcrack densities were determined from the total number of microcracks counted along two adjacent 25 mm edges of each specimen. Only transverse

cracks extending across at least three-quarters of a ply were included in the density calculations, following the criterion proposed by Bechel and Kim [39] and also used by Saha *et al.* [23]. After 100 cycles, no cracks had formed in either edge 1 or edge 2 in any of the three modified CFRE specimens cycled, as shown in Figure 3c and g for TC_3. However, by 250 cycles, cracks had formed in five of the six inspected edges, as illustrated in Figure 3d, in which one transverse crack was observed in the central 90° layer of edge 1 and in Figure 3h, where two cracks were observed in the 90° surface plies in edge 2.

In our previous work, thermal cycling using the unmodified epoxy as the CFRE matrix was reported, with cracks appearing as early as the first cycle in edge 2 of one specimen [9]. Figure 4 presents a plot of crack density as a function of the cycle number for the unmodified and modified CFRE. As shown in Figure 4, the crack density increases at every cycle increment for the unmodified CFRE, reaching 0.47 cracks per centimetre by 100 cycles. In comparison, the modified matrix exhibited no cracking by 100 cycles. After 250 cycles, the crack density of the unmodified CFRE was 2.06 cracks per centimetre, while the modified CFRE was 58% lower, with 0.87 cracks per centimetre. Comparison with the literature on in-house matrix-modified CFRE laminates is not straightforward, due to differences in manufacturing method, lay-up and thermal cycling conditions, all of which can influence cryogenic matrix microcracking. Several studies on modified CFREs reported effective crack mitigation in $[0/90_4]_s$ laminates produced via VARTM after a single 45 min immersion in liquid nitrogen [29-31], while other studies reported reduced crack density after a small number of cycles between −196 °C and RT [33, 36, 37]. In work extending to 200 cycles between -196 °C and RT, matrix modification was shown to reduce crack density even when cracking initiates early in the cycling sequence [32]. The present results add to this literature by showing suppressed cracking up to 100 cycles and reduced crack density after 250 cycles between −196 °C and +55 °C, compared with the unmodified CFRE.

Journal Pre-proof

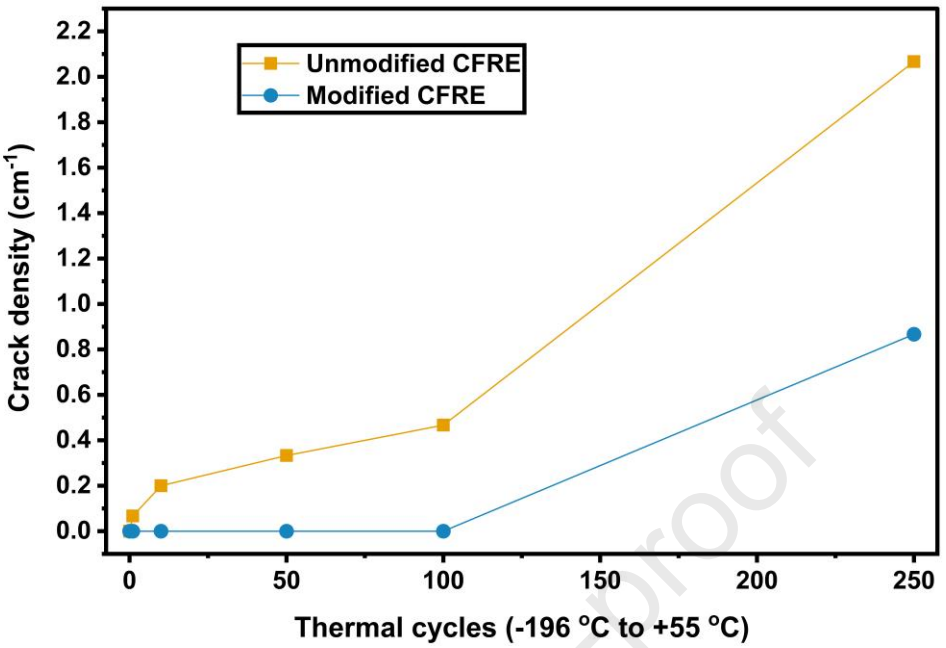


Figure 4: Crack density following thermal cycling between −196 °C and +55 °C for the unmodified and modified CFRE.

3.2. Effect of microcracking on hydrogen permeability

To investigate how the thermally induced cracking affected the hydrogen (H_2) permeability of the modified CFRE, 0-cycle (uncracked) and 250-cycle (cracked) specimens were subjected to room temperature H_2 permeability experiments, with the results detailed in Table 1. Additional H_2 permeation repeats were attempted, however, given the technical challenges associated with this kind of testing, only a limited number of tests produced datasets suitable for analysis. The results are therefore interpreted as trends in transport behaviour rather than definitive absolute permeability values.

Table 1: Hydrogen permeability data for 0-cycle (uncracked) and 250-cycle (cracked) modified CFRE specimens.

Specimen	*Thermal cycles*	*Edge crack density (cm^{-1})*	*Thickness (mm)*	*Permeation area (mm^2)*	*Time lag (h)*	*Permeability coefficient [$x10^{-16}$ mol·m/(m^2·s·Pa)]*	*Diffusion coefficient [$x10^{-11}$ m^2/s]*	*Solubility coefficient [$x10^{-6}$ mol/(m^3·Pa)]*
TC_1	0	0.0	2.40	158	16.31	1.33	1.64	8.11
TC_2	0	0.0	2.42	157	14.58	1.48	1.86	7.98
TC_3	250	0.6	2.44	177	10.56	1.58	2.61	6.06
TC_4	250	1.6	2.47	149	9.29	2.33	3.05	7.63

Following 250 thermal cycles, the mean H_2 permeability coefficient increased from 1.41 ± 0.11 × 10^{-16} mol·m/(m^2·s·Pa) for the uncycled specimens to 1.96 ± 0.53 × 10^{-16} mol·m/(m^2·s·Pa), while diffusivity increased from 1.75 ± 0.16 × 10^{-11} m^2/s to 2.83 ± 0.31 × 10^{-11} m^2/s, with greater scatter in the thermally cycled specimens. In contrast, solubility remained of similar magnitude across all samples. Although the small number of valid tests means that these values should be interpreted as preliminary trends, the increase in diffusivity suggests that the higher permeability is associated primarily with damage assisted transport through the laminate rather than a substantial change in polymer–gas thermodynamic interactions caused by the thermal cycling. This is also reflected in the measured time lag (t′), which decreased from 15.45 ± 1.22 h in the uncycled specimens to 9.93 ± 0.90 h in the cycled specimens. The individual pressure–time curves for each valid permeation test are shown in Figure 5 and exhibited a clear time lag followed by a linear steady-state region, consistent with Fickian transport behaviour under the conditions tested. This characteristic supports reporting the present data in terms of permeability, diffusivity and solubility, rather than as leak rate, since permeability values derived from Fick's law are only meaningful in damaged composites where Fickian behaviour is retained [45]. Although permeability is reported here following the principles in ISO 15105, the authors recognise that for fibre-reinforced laminates exhibiting thickness-dependent microcracking, permeance may be a more appropriate descriptor when comparing laminates of substantially different thicknesses, because thickness can influence the extent and connectivity of cracking and, consequently, the total gas transmitted through the laminate [45]. In the present study, specimen thickness varied only marginally (2.40–2.47 mm) and all specimens were derived from the same laminate; the observed trends are therefore attributed primarily to differences in damage state rather than thickness effects.

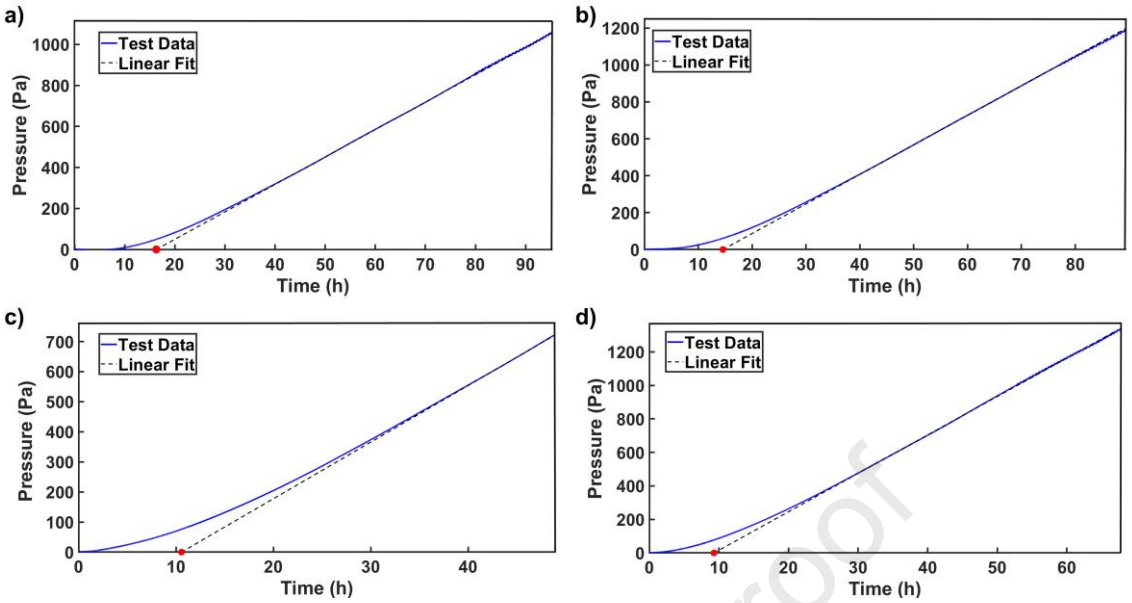


Figure 5: Individual H_2 pressure–time permeation curves for a) TC_1 and b) TC_2 after 0 cycles and c) TC_3 and d) TC_4 after 250 thermal cycles between −196 °C and +55 °C.

The relationship between microcrack density and transport coefficients is illustrated in Figure 6. TC_3 (0.6 cracks cm^{-1}) exhibited a 12% increase in permeability and a 49% increase in diffusivity relative to the uncycled mean, whereas TC_4 (1.6 cracks cm^{-1}) showed larger increases of 66% and 74%, respectively. Potential sources of scatter in H_2 permeation experiments can include sealing integrity, system stability and specimen-to-specimen inhomogeneity. Specimen variability was reduced by testing specimens taken from the same laminate, while sealing and system-related effects were controlled using deformable indium seals, a separate side chamber to assess seal integrity and detect lateral gas leakage, vacuum-decay testing, baseline leak-rate correction and positive-pressure leak checks. Differences in local damage state are also reflected in the observed scatter, with the higher permeability of TC_4 coinciding with its greater edge crack density, suggesting that the variation between the thermally cycled specimens is at least partly related to differences in microcracking.

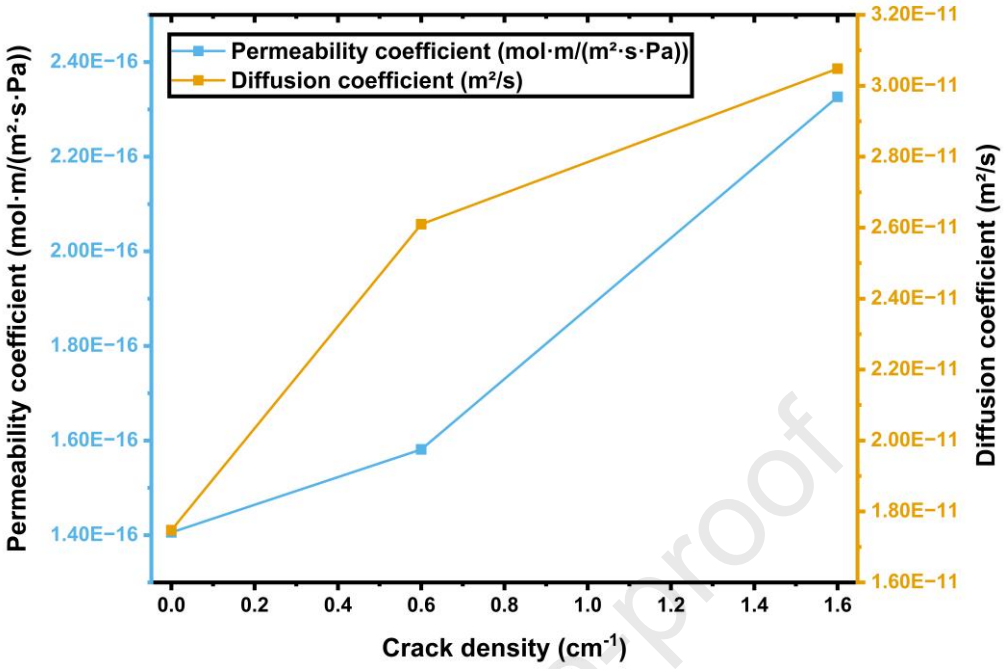


Figure 6: Permeability and diffusion coefficient as a function of edge crack density.

This trend is consistent with a damage-assisted transport mechanism, in which increasing microcrack density may reduce laminate tortuosity and thereby increase H_2 transport, primarily through higher diffusivity. This is consistent with previous studies reporting that increased thermal cycling leads to greater matrix microcracking and corresponding increases in gas permeability [19-21], although those studies used helium (kinetic diameter *ca.* 260 pm) rather than hydrogen (kinetic diameter *ca.* 289 pm). The crack densities in Table 1 were measured by optical microscopy along two adjacent polished specimen edges, as described in Section 3.1. They should therefore be viewed as edge-based indicators of relative damage state, rather than direct measurements of internal crack volume within the reduced permeation area. Even so, the clear difference in crack density between the two cycled specimens provides useful context for the corresponding changes in transport behaviour. However, once an interconnected crack network forms through the laminate thickness, transport may transition from permeability-controlled diffusion to leakage, for which the resulting flux can be orders of magnitude higher than that associated with permeation, as discussed by Koord *et al.* [24]. The Fickian behaviour of the pressure-time data in Figure 5 suggests that transport in the cracked specimens

remained diffusion-controlled under the test conditions, rather than *via* leakage through an interconnected crack network from one face to the other. To further investigate this, xCT was carried out on the cracked specimens, given its established value for assessing internal laminate damage, including intra-ply cracking, in composite laminates [46]. Figure 7 presents representative 3D reconstructions of TC_3 and TC_4.

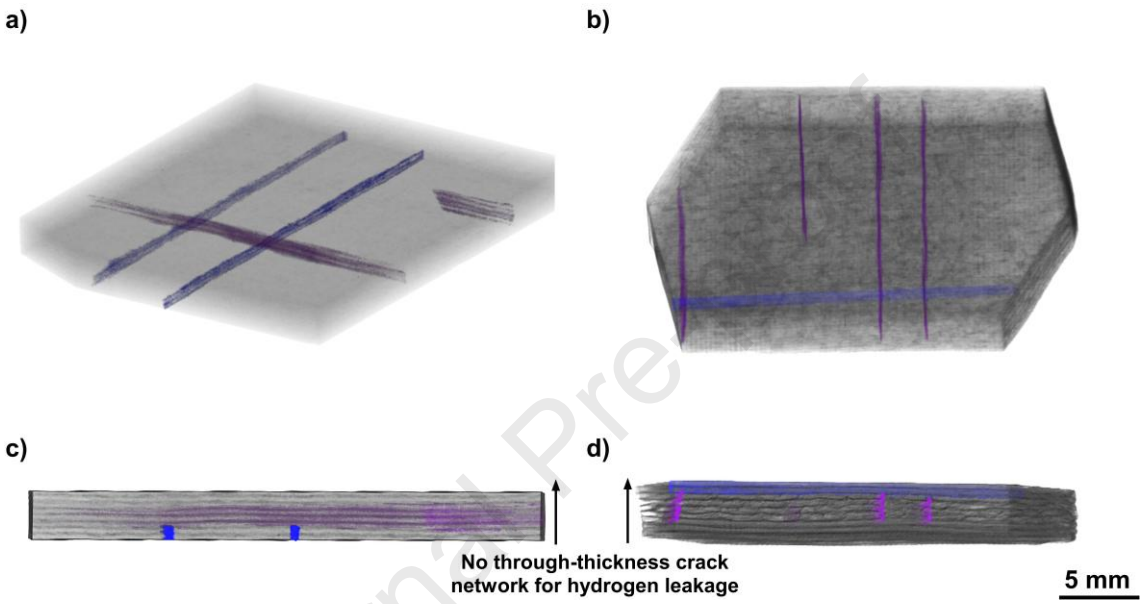


Figure 7: 3D xCT volume renderings of a), c) TC_3 and b), d) TC_4. Cracks shown in purple are transverse to the fibre direction in the inner 90° plies, while cracks shown in blue are located in the outer 0° plies.

In TC_3, two cracks were resolved in the same outer 0° plies and two within the inner 90° block, one of which extended only a small distance along the specimen length. In TC_4, one crack was resolved in the outer plies and four within the inner 90° block, with two of the latter extending only part way along the specimen. In both specimens, the resolved cracks occupied only part of the laminate thickness, and no continuous through-thickness crack path was observed in the xCT reconstructions. This is consistent with the Fickian behaviour of the permeation curves in Figure 5. However, the xCT scans resolved only the larger cracks spanning the blocked 90° plies or outer 0° plies. Smaller cracks identified by optical microscopy, including those used in the crack density values in Table 1, Figure 4 and Figure 6, could not be resolved at the available xCT resolution, even when the field of view was reduced to the smallest practical area around the reduced permeation zone. Given their limited extent, with the

Journal Pre-proof

optical crack-density criterion including cracks extending across at least three-quarters of a ply, and the fact that the H_2 permeation curves remained Fickian, these smaller cracks are not thought to form an interconnected leakage path from one face of the specimen to the other. They are, however, likely to contribute to the increase in H_2 transport by increasing the local void space available for diffusion and thus the effective diffusivity.

The xCT reconstructions therefore show that cracking extended into the specimen interior and was not confined to the polished edges. They also provide information that could not be obtained from 2D edge observations alone, reinforcing the need for correlative damage assessment in microcracked laminates. This agrees with previous leakage work, where correlating leak rate with damage state required quantitative leak measurement alongside complementary assessment of laminate damage using edge inspection and polished cross-sections [27]. In the present study, the three cracks visible optically in TC_3 were all identified in the xCT reconstruction, while the scan also revealed a further transverse crack that propagated only part way into the specimen and was therefore not visible on the polished edge. This highlights the value of xCT in identifying partial internal cracks that do not intersect a 2D surface, while also illustrating the difficulty of resolving cracks of only a few tens of microns within specimens of millimetre-scale thickness and centimetre-scale length.

3.3. Thermal loading and microscale damage formation

Our previous work demonstrated the use of cryo-SEM to visualise microscale damage formation in an unmodified CFRE under both controlled cooling and thermal shock via cryogenic immersion. Under both regimes, widespread damage was observed, including fibre–matrix debonding and microscale matrix cracking, which likely acted as initiation sites for the larger transverse matrix cracking detected after a single thermal cycle and contributed to the 76% reduction in stress at first crack [9]. Given that no transverse cracking was observed in the modified CFRE up to 100 cycles, as discussed in Section 3.1, this raised the question of whether similar microscale damage was forming in the modified system. To subject the modified CFRE to thermal shock *via* rapid cooling, a 3 mm x 5 mm specimen was immersed in slush

Journal Pre-proof

nitrogen (SN_2, ~−207 °C). Identical regions were imaged before and after immersion, with post-immersion scans acquired at −130 °C using the SEM cryo-stage. Figure 8a shows area 1 prior to immersion and Figure 8b after immersion at −130 °C. Further examples are presented in Supplementary Figure S3.

In contrast to the unmodified CFRE, no matrix cracking or fibre–matrix interfacial debonding was observed following immersion. Although the matrix and interfaces remained intact, several new fibre cracks were visible after immersion, highlighted by the blue arrows in Figure 8b and Supplementary Figure S3d. Comparison with the corresponding pre-immersion cross sections in Figure 8a and Supplementary Figure S3c suggests that many of these cracks formed in fibres that previously appeared undamaged. However, the cross sections marked by the yellow arrows indicate that fibres containing pre-existing defects exhibited further damage, suggesting that thermal shock can exacerbate existing fibre defects. Within this system, the retention of matrix and fibre–matrix interfacial integrity alongside fibre cracking highlights the robustness of the modified matrix under cryogenic thermal shock. These findings suggest that, under these conditions, the fibres may be the more susceptible constituent during cooling, as further discussed in Section 3.4, whereas the matrix and fibre–matrix interfaces remain comparatively resistant to damage formation.

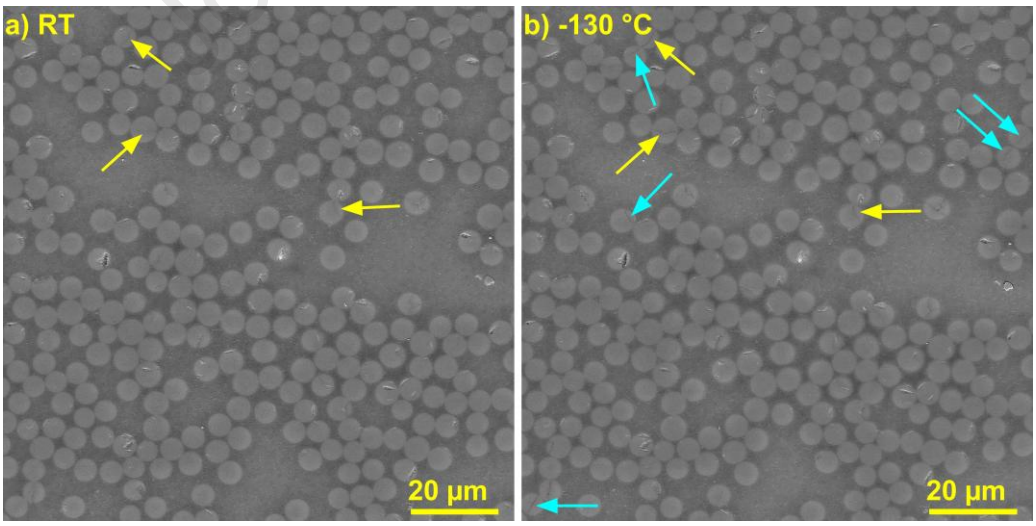


Figure 8: SEM micrographs of a) area 1 pre-immersion and b) area 1 post-immersion in slush nitrogen (~−207 °C) and imaged at −130 °C using a cryo-SEM stage. No damage was observed in the matrix or fibre–matrix interface post-immersion, but new fibre cracks were observed (blue arrows), and pre-existing fibre damage was exacerbated (yellow arrows). Additional examples are shown in Supplementary Figure S3.

In our previous work, slow cooling had a more pronounced effect on microscale damage formation in the unmodified CFRE, with 94% of the fibres in the SEM field of view exhibiting some degree of fibre–matrix debonding across 331 observed fibre cross-sections [9]. To investigate whether the modified matrix had similar resilience to slow cooling as it did with thermal shock, the modified CFRE was cooled *in-situ* in the SEM chamber at ~6 °C min^{-1} to −138 °C, held for around 9 minutes then rewarmed at ~2 °C min^{-1}. *In-situ* cryo-SEM enables continuous imaging during controlled cooling and re-warming, allowing detailed microscale damage initiation and growth to be tracked in real time at substantially higher spatial resolution than X-ray-based approaches that primarily resolve larger internal defects. Video 1 compiles 721 SEM images recorded during the thermal cycle, shown alongside the corresponding temperature profile, focusing on a local region within the central 90° ply block at the polished specimen edge. In Figure 9, individual micrographs taken from the sequence at distinct temperatures are presented.

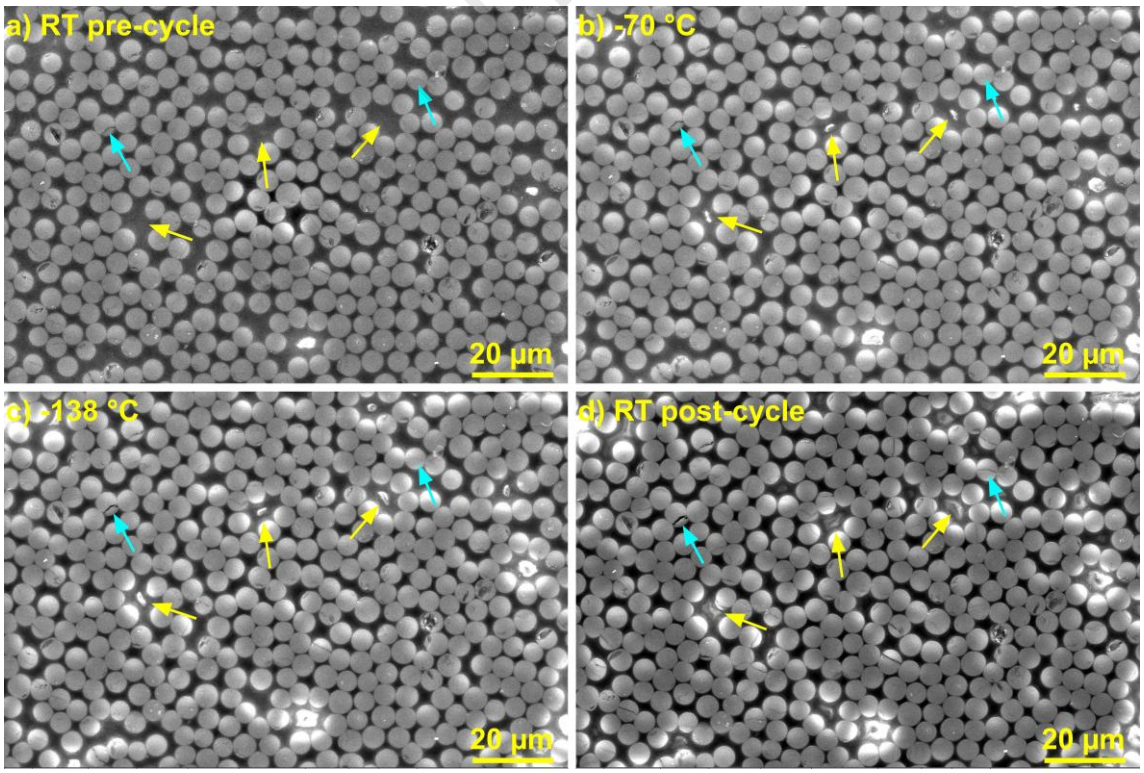


Figure 9: SEM micrographs acquired during gradual cooling of the modified CFRE: a) RT pre-cycle; b) −70 °C; c) −138 °C at the lowest temperature during the thermal cycle and d) at RT post-cycle. Yellow arrows indicate areas of matrix deformation and blue arrows indicate exacerbation of fibre defects. The full sequence of 721 SEM images is shown in Video 1 alongside a corresponding temperature profile.

Across the sequence in Figure 9a-d, no matrix cracking or fibre–matrix debonding was observed at any stage of the thermal cycle. In the room temperature pre-cycle image (Figure 9a), the fibres are uniformly embedded within the modified epoxy matrix, the interfaces appear intact, and several fibres exhibit pre-existing defects within their cross-sections. As the specimen is cooled to −70 °C (Figure 9b) and then to −138 °C (Figure 9c), contrast changes appear within the resin-rich regions between fibre clusters, with examples highlighted by the yellow arrows. Given the use of a secondary electron detector, which is sensitive to surface topography, these evolving bright and dark regions are attributed to deformation associated with constrained thermal contraction of the matrix within the fibre reinforcement, as the temperature is decreased [47]. The features are diffuse rather than sharply defined, and no interfacial gaps or crack-like discontinuities are observed, indicating that the matrix accommodates the thermal strain without fracturing. During cooling, several fibres with pre-existing defects show clear worsening of those flaws at low temperature, with examples highlighted by the blue arrows. These cracks remain confined to the fibres and did not propagate into the adjacent matrix or lead to interfacial debonding. After rewarming to room temperature (Figure 9d), much of the matrix contrast variation diminishes (yellow arrows), indicating partial recovery of the thermally induced surface relief, whereas the fibre cracks persist and in some cases are worsened (blue arrows). Overall, slow cooling to −138 °C leads to partially reversible deformation within the modified epoxy matrix but irreversible damage within susceptible fibres, while the fibre–matrix interfaces remain intact. This suggests that local strain accumulation within susceptible fibres may contribute to the observed fibre damage. This interpretation is considered further in Section 3.4, in the context of X-ray diffraction (XRD) based measurements showing that transverse lattice strain develops within embedded carbon fibres during cooling [7]. The damage evolution in the modified CFRE is in clear contrast to the unmodified CFRE, which, despite being cooled only to −85 °C, exhibited severe microstructural damage, as shown in the higher-magnification post-mortem images of both materials acquired at room temperature after the thermal cycle (Figure 10).

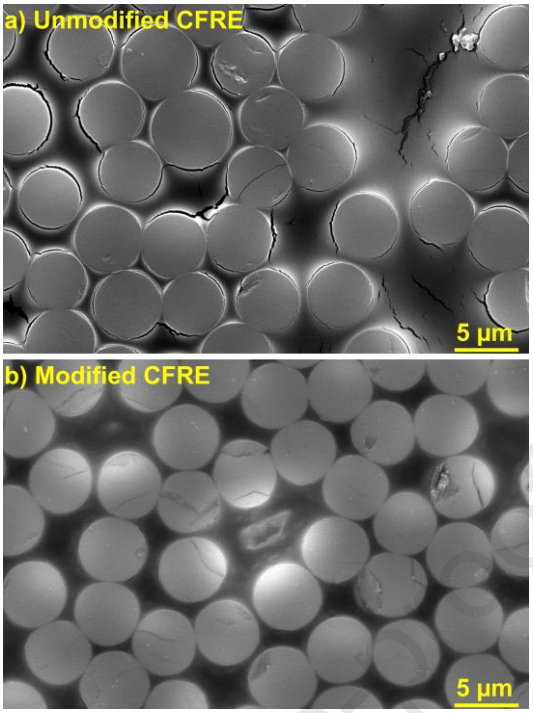


Figure 10: SEM images acquired at room temperature after one thermal cycle: a) unmodified CFRE, showing widespread microscale damage, including matrix cracking and fibre–matrix debonding (adapted from [9]); and b) modified CFRE, showing localised matrix deformation but no evidence of fibre–matrix interfacial debonding or matrix cracking.

Consistent with our earlier observations, slow cooling in the present study produced a more pronounced effect on the microscale morphology of the modified CFRE than thermal shock. The extended thermal exposure during gradual cooling provided sufficient time for strain to accumulate as a result of the transverse contraction mismatch between the higher-CTE matrix and the carbon fibres, leading primarily to areas of matrix deformation. In contrast, rapid immersion imposed abrupt thermal loading, generating steep temperature gradients over a very short time interval; despite this sudden temperature change, no comparable matrix deformation was observed. Importantly, during gradual cooling, these changes were diffuse rather than discrete fracture features, with no matrix cracking or fibre–matrix interfacial debonding observed in the modified CFRE, unlike in the unmodified CFRE. Together with the partial recovery of matrix contrast after rewarming, this suggests that cooling-induced strain was accommodated locally within the modified matrix rather than being relieved through matrix fracture or fibre–matrix interfacial separation. Although only local regions of the specimens were captured in the SEM field of view, the lack of visible microscale matrix cracking or debonding suggests fewer

crack-initiation sites in the modified CFRE, helping to explain the delayed onset of larger transverse cracks during thermal cycling compared with the unmodified CFRE.

Despite the higher measured CTE of the modified epoxy, of 66.4 μm/(m·°C), compared to 55.4 μm/(m·°C) for the unmodified epoxy, the greater CTE mismatch between the fibres and matrix did not translate into increased damage. This indicates that CTE mismatch alone does not dictate damage initiation in this system. Rather, the modified matrix appears capable of accommodating thermally induced strain without generating the localised stress concentrations required for matrix cracking or interfacial debonding. This suggests that although epoxy toughening with particles such as CSR can lose effectiveness at low and cryogenic temperatures as behaviour becomes increasingly matrix-dominated [48], incorporating components with low glass transition temperatures could be advantageous when modifying an epoxy matrix and should be considered alongside efforts to limit CTE mismatch when designing cryogenic matrices. In the modified epoxy, the MX-150 additive containing polybutadiene-based CSR particles (core T_g = −76 °C [48]) and the long-chain aliphatic segments in EPS35 (T_g = −20.6 °C [38]) may help accommodate strain at reduced temperature.

3.4. FIB-SEM investigation of fibre damage

While cryo-SEM observations showed that matrix cracking and fibre–matrix interface debonding on cooling were suppressed in the modified CFRE, both fibre cracking and the exacerbation of pre-existing fibre defects were observed in the unmodified CFRE [9] and modified CFRE. Such fibre damage associated with cryogenic exposure is rarely reported, as thermally induced damage in CFRP is typically concentrated within the matrix and at the fibre–matrix interface. Where fibre damage has been observed, it is generally linked to the propagation of transverse cracks rather than occurring in isolation; for example, Timmerman reported fibre splitting during transverse crack growth in nanoclay-modified CFRE laminates under cryogenic cycling [37].

To provide a mechanistic follow-up to the fibre damage observed during cryogenic exposure, focussed ion beam (FIB) milling was carried out on fibres within the unmodified CFRE

to determine whether isolated surface cracks were confined to the polished cross-section or extended into the fibre interior. Figure 11 illustrates the workflow used for these experiments. First, a large cross was milled into the polished edge of a 3 mm × 5 mm specimen using argon ion milling. This cross served as a positional reference to allow the same region to be relocated following thermal cycling. A series of SEM images were then collected across the region of interest and stitched together to produce a large-area map of the specimen edge. Figure 11a shows a section of this stitched image, with Figure 11b highlighting a fibre that was later found to sustain cryogenic damage. The specimen was then removed from the chamber and subjected to ten thermal cycles by repeated immersion in LN_2 followed by warming to room temperature. After cycling, the specimen was returned to the SEM chamber, and the previously acquired stitched image map was used to relocate the same region of the polished edge. The new SEM images were compared with the original stitched dataset to identify fibres that had sustained damage during thermal cycling. Figure 11c shows one such fibre, where a small wedge-shaped surface crack developed as a result of the thermal cycling. To investigate whether this damage extended into the fibre interior, the SEM stage was tilted by 52° and a thin protective layer of platinum was deposited over the fibre surface (Figure 11d). FIB milling was then performed transverse to the fibre axis to progressively expose the fibre cross-section beneath the damaged region. Figure 11e-g show the progression of milling, revealing that in this instance the damage was confined to the fibre surface and did not extend into the fibre interior.

Journal Pre-proof

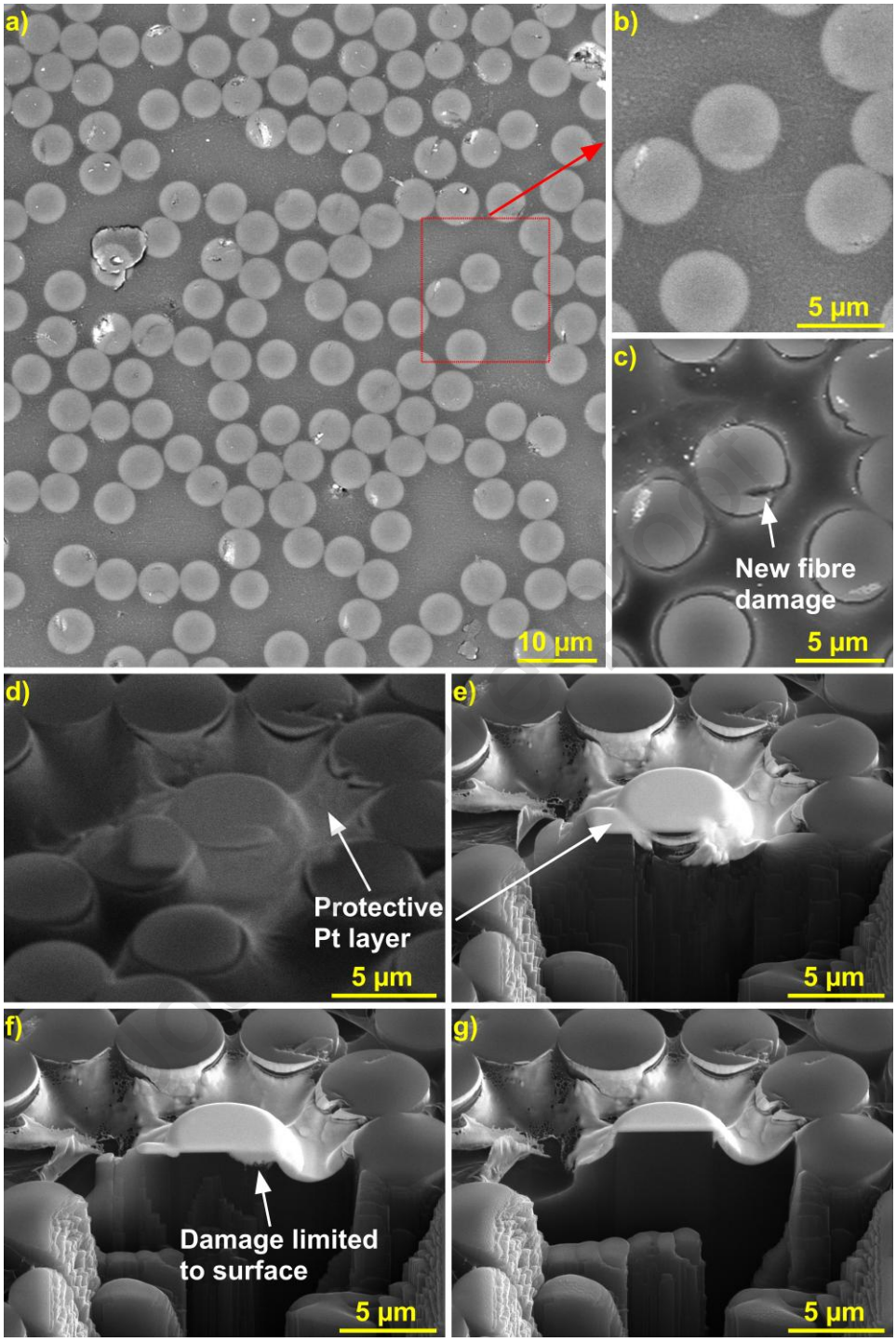


Figure 11: SEM images of the workflow used to investigate fibre damage formed during thermal cycling of the unmodified CFRE: a) identification of a region of interest (ROI); b) higher magnification of the ROI prior to thermal cycling; c) the ROI post-cycling with fibre damage identified; d) protective platinum (Pt) layer being applied to the fibre surface; e–g) FIB milling.

The same workflow was repeated on a second fibre, as shown in Figure 12. Figure 12a and b show the fibre before and after thermal cycling, respectively, where a similar wedge-shaped surface crack is visible. During subsequent FIB milling, a narrow hairline feature became visible

extending from the base of the wedge crack into the fibre (Figure 12c). For clarity, the matrix, fibre and fibre–matrix interface are labelled in the milled pillar.

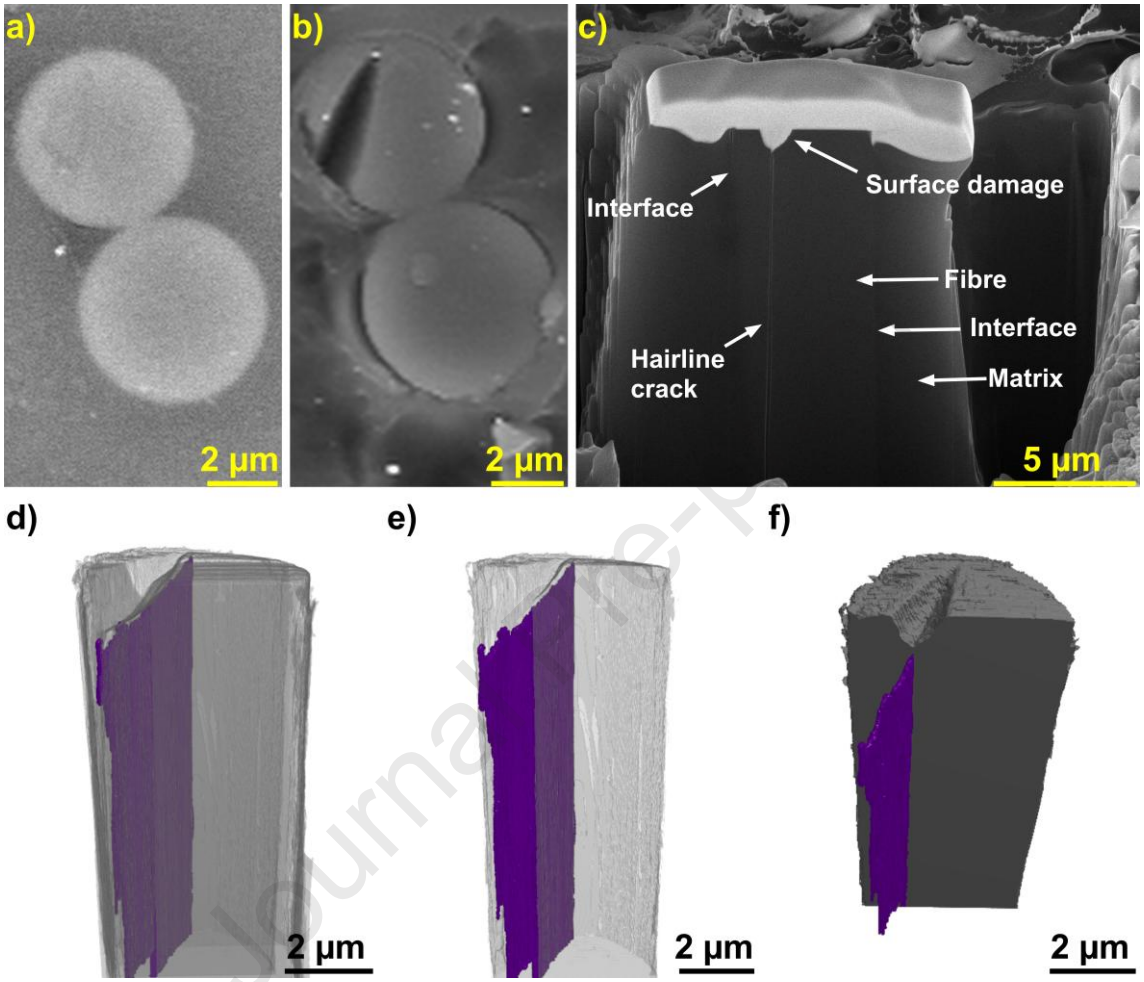


Figure 12: SEM images showing a) the region of interest (ROI) prior to thermal cycling of the unmodified CFRE; b) the same ROI following thermal cycling; c) focussed ion beam (FIB) milling of the damaged fibre, with the fibre, matrix and fibre–matrix interface indicated and revealing a hairline crack within the fibre interior. d-f) 3D reconstruction from the FIB–SEM dataset showing the crack (purple) within the fibre (grey).

One possible explanation for such features during FIB preparation is curtaining, a common milling artefact that appears as streaks on the milled surface due to differential sputtering rates during ion beam removal [49]. This is common in multiphase materials such as composites, where milling rates can vary due to the local variation of material characteristics in different phases [50]. In the present case, however, the feature observed here is unlikely to be curtaining, as it is not aligned with the milling direction, appears as a single discrete feature

Journal Pre-proof

rather than periodic streaking, and is confined to the fibre rather than extending across both fibre and matrix. Segmentation of the FIB-SEM image stack showed a narrow planar hairline crack within the fibre interior, located beneath the surface wedge crack and running broadly along the longitudinal axis of the fibre (Figure 12d–f). Carbon fibres can also exhibit internal thermal expansion mismatch within their microstructure: the highly oriented fibre core typically exhibits a negative axial coefficient of thermal expansion, causing it to expand along the fibre axis during cooling, while the outer, amorphous regions exhibit a more disordered structure and positive coefficient of thermal expansion [1, 51]. Cooling to cryogenic temperatures can therefore generate internal stresses between the core and outer regions of the fibre, with previous work by Zhang *et al.* reporting increased fibre surface roughness following cryogenic exposure, attributed to cracking and partial loss (“shelling off”) of the outer layer [52]. In that study the fibres were cryogenically treated without a surrounding matrix and the observed reduction in fibre diameter with increasing treatment time was attributed to progressive removal of this outer disordered layer. In the present study, the fibres are embedded within an epoxy matrix, introducing an additional constrained thermal strain state during cooling.

Recent XRD measurements by Srisuriyachot *et al.* showed that PAN-based carbon fibres develop measurable transverse lattice strain on cooling, and that this strain is greater in embedded fibres than in dry fibres due to constraint from resin contraction. At −70 °C the reported transverse fibre strain increased from approximately −2700 με in dry fibres to −3000 με in a quasi-isotropic CFRP laminate and −3700 με in a unidirectional CFRP laminate [7]. Although measured over a less severe temperature range than the present cryogenic cycling experiments, these findings demonstrate that the fibre lattice is itself strained during cooling, with greater deformation expected at lower temperatures. The hairline crack observed in the present study may therefore be associated with local strain accumulation in the fibre, particularly where microstructural heterogeneity acts as a stress concentrator. However, it should be noted that although the surface wedge crack was generated during thermal cycling, it cannot be determined with certainty whether the internal hairline crack formed during cycling or represents a pre-existing flaw within the fibre. This uncertainty arises because FIB-SEM is a destructive technique and prevents internal imaging of the same fibre both before and after

thermal exposure. Within the current study, the purpose of the FIB-SEM analysis was to determine whether surface fibre damage observed after thermal cycling was confined to the polished cross-section or extended into the fibre interior. A systematic comparison of uncycled and thermally cycled fibres would therefore be valuable in future work to determine whether such internal features are pre-existing or develop during cryogenic exposure.

3.5. Temperature-dependent fracture behaviour of the matrix

The cryo-SEM observations in Section 3.3 showed that microscale matrix cracking and fibre–matrix debonding were suppressed in the modified CFRE, despite the increased CTE mismatch between the modified matrix and carbon fibres. However, these observations do not establish whether the matrix itself has greater resistance to crack growth at cryogenic temperature. To isolate the temperature-dependent fracture behaviour of the matrix, the neat resins were therefore evaluated using SENB testing at +23 °C and −196 °C, with the results summarised in Table 2.

Table 2: SENB data for the unmodified and modified epoxy.

	K_{IC} (MPa·m$^{1/2}$)		G_{IC} (kJ/m^2)	
	+23 °C	**−196 °C**	**+23 °C**	**−196 °C**
Unmodified epoxy*	1.17 (±0.09)	2.86 (±0.20)	0.47 (±0.06)	2.34 (±0.34)
Modified epoxy	2.60 (±0.05)	2.70 (±0.04)	2.75 (±0.08)	2.57 (±0.28)

** Data for the unmodified epoxy are reproduced from [9].*

As previously reported, the unmodified epoxy exhibited a strong temperature dependence: fracture toughness (K_{IC}) increased from 1.17 to 2.86 MPa·m$^{1/2}$ and fracture energy G_{IC} from 0.47 to 2.34 kJ/m^2 at −196 °C [9]. This fracture behaviour is typical of unmodified, crosslinked thermosets, where reduced free volume within the network on cooling brings polar functional groups closer together, increasing intermolecular forces and the polymer's resistance to crack propagation [53-55]. On the other hand, the modified epoxy showed minimal change with temperature. K_{IC} remained effectively constant (2.60 to 2.70 MPa·m$^{1/2}$), and G_{IC} varied only slightly (2.75 to 2.57 kJ/m^2), remaining within experimental scatter.

Optical and SEM images of fracture surfaces from SENB specimens tested at −196 °C and +23 °C are shown in Figure 13. At both temperatures, the unmodified epoxy exhibits smooth fracture surfaces in the optical images (Figure 13a, c), with river lines evident in the corresponding SEM micrographs (Figure 13e, g), indicative of brittle, unstable crack propagation. For the modified epoxy at −196 °C, the optical image appears relatively smooth (Figure 13b), while the SEM micrograph reveals an angular, stepped fracture surface with grain-like morphology (Figure 13f). At +23 °C, the modified epoxy shows pronounced stress whitening and a rough fracture surface in the optical image (Figure 13d), consistent with increased toughness compared to the unmodified epoxy at the same temperature, with the corresponding SEM micrograph displaying a rough, tortuous morphology (Figure 13h).

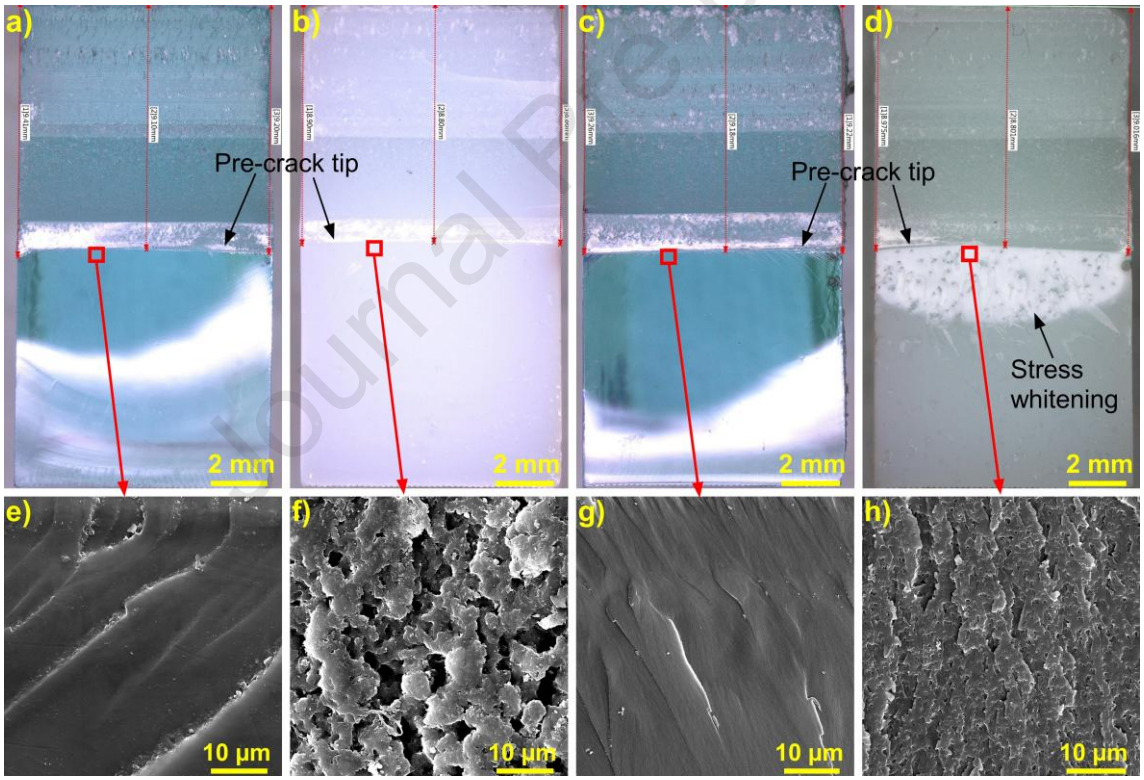


Figure 13: Optical microscopy images of SENB fracture surfaces for a) unmodified epoxy at −196 °C; b) modified epoxy at −196 °C; c) unmodified epoxy at +23 °C; and d) modified epoxy at +23 °C, with e–h) corresponding SEM micrographs of the fracture surfaces.

Figure 14 presents high-resolution SEM images of the fracture surfaces of the modified epoxy at −196 °C and +23 °C. These images were selected from regions representative of the

fracture-surface morphologies observed across the tested specimens. At −196 °C (Figure 14a), the fracture surface exhibits CSR particle debonding and pull-out, evidenced by well-defined cavities and relatively smooth cavity walls, indicative of interfacial failure with limited matrix deformation. In contrast, at +23 °C (Figure 14b), the irregular, enlarged voids and localised matrix deformation are consistent with CSR particle cavitation and plastic void growth, as reported for rubber-toughened epoxy fracture mechanisms [56-58]. While the measured fracture properties remain relatively stable between the two temperatures, the contribution from particle-related toughening diminishes at cryogenic temperature. The epoxy network therefore has a greater influence on the fracture response, as reflected by the temperature-dependent changes in K_{IC} and G_{IC} observed in the unmodified epoxy.

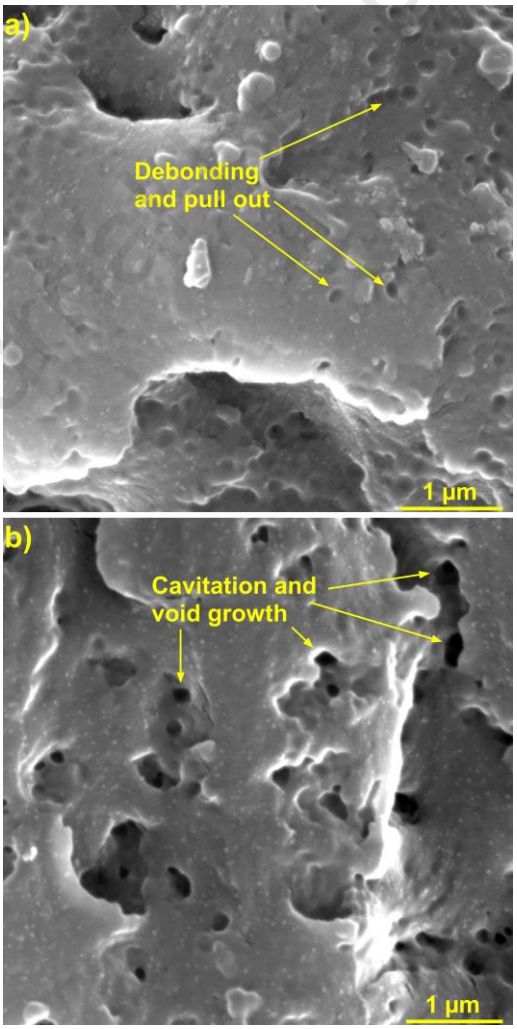


Figure 14: SEM images of the modified epoxy SENB fracture surfaces at a) −196 °C, showing particle debonding and pull-out, and b) +23 °C, showing cavitation and plastic void growth.

Journal Pre-proof

3.6. Transverse cracking under combined thermo-mechanical loading

Although resistance to thermally induced microcracking is important for cryogenic composite applications, tank structures must also withstand combined thermal and mechanical loading without transverse cracking. To investigate the capacity of the CFRE to do this, quasi-static tensile tests were conducted at both room and cryogenic temperatures, with *in-situ* video recording of cross-sectional damage as load was applied. Figure 15 presents a series of video stills at the applied loads when cracks formed, for representative specimens of the unmodified (Figure 15a) and modified CFRE (Figure 15b) at −155 °C, with the images for the unmodified CFRE specimen adapted from [9]. The final image on the right of each series shows the damage state just prior to failure and the yellow arrows indicate the first transverse crack forming in each case, at the respective applied tensile stress.

Journal Pre-proof

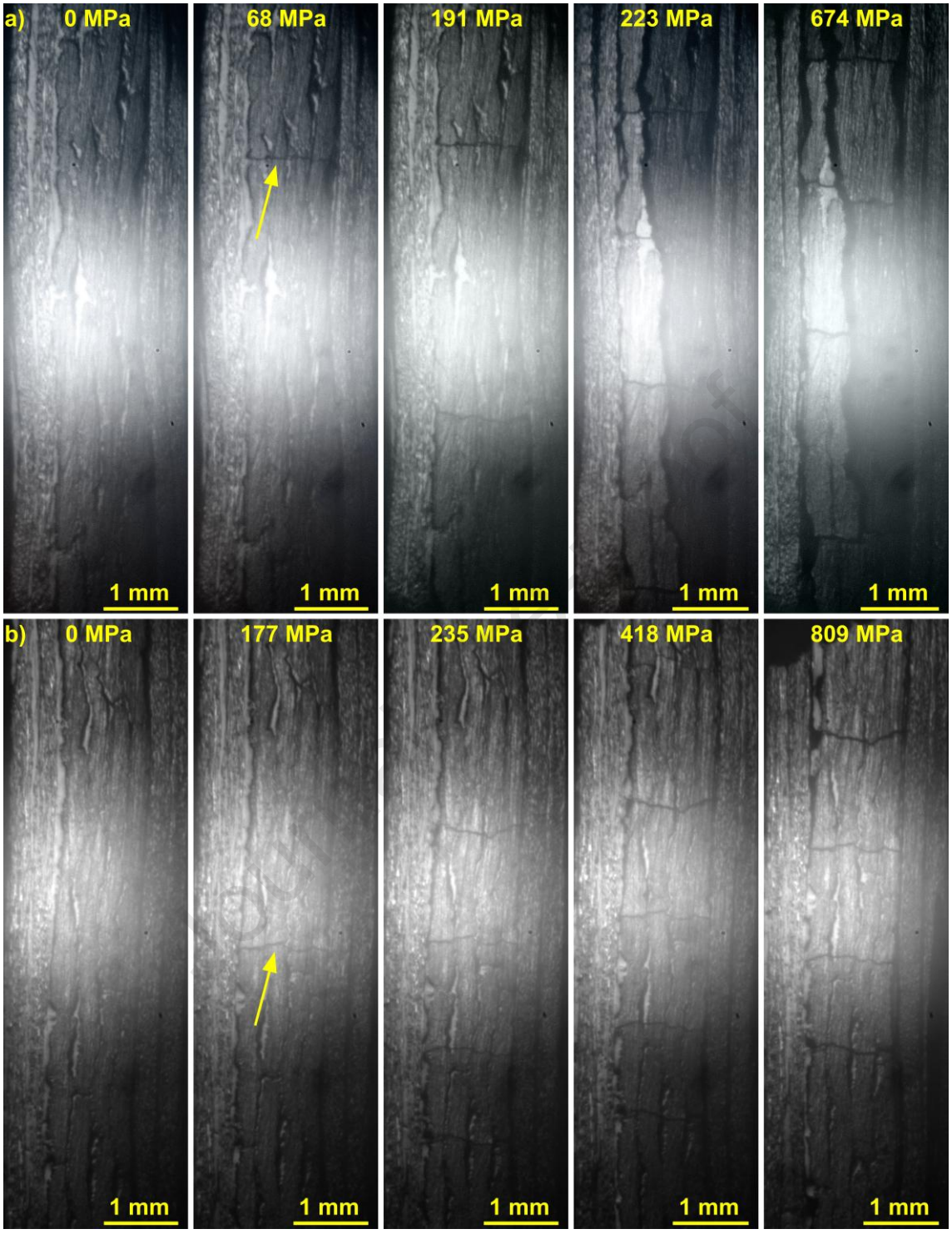


Figure 15: Video frames of transverse microcrack development and delamination with applied tensile stress, for a) the unmodified CFRE at −155 °C, adapted from [9] for comparison with b) the modified CFRE at −155 °C. The yellow arrows indicate the first transverse crack formed at the corresponding applied stress, with the final frame on the right of each series depicting the extent of damage just prior to failure. Experimental results for all specimens tested are included in Supplementary Table S1.

Journal Pre-proof

As shown in Figure 15a, the first microcrack appeared at 68 MPa in this unmodified CFRE specimen with further cracks and significant delamination appearing until failure at 674 MPa. In the modified CFRE specimen (Figure 15b), the first crack was observed at 177 MPa, with further cracks forming until failure at 809 MPa. Figure 16 shows the evolution of transverse crack density with applied stress for both CFREs at +23 °C and −155 °C. Each data point corresponds to the formation of one or more additional cracks at a given stress, with full experimental details provided in Supplementary Table S1.

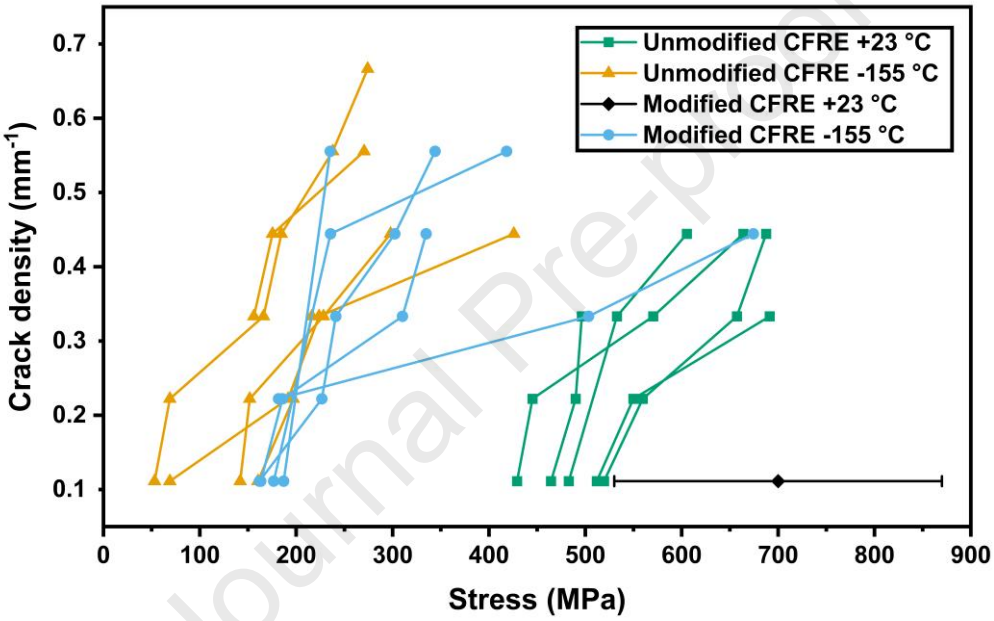


Figure 16: Transverse crack density as a function of applied tensile stress, for the unmodified and modified CFRE at +23 °C and −155 °C. Each coloured trace corresponds to an individual specimen within the indicated material and temperature condition. The black marker with horizontal bar indicates the start and completion of stable propagation of the only fully transverse crack observed in the modified CFRE at +23 °C, whereas all other data points correspond to instantaneous transverse crack formation. The data for each specimen at both temperatures is included in Supplementary Table S1.

In the unmodified CFRE specimens at +23 °C and −155 °C and modified CFRE specimens at −155 °C, cracks formed instantaneously as tensile stress was increased, while in contrast, the modified CFRE at room temperature exhibited very different behaviour, with four of five specimens showing no cracking within the gauge length prior to failure. In the remaining specimen, depicted in Supplementary Figure S4, a single crack initiated at approximately 530 MPa, with local 0°/90° delamination also visible, before propagating by stable, tortuous growth to traverse the blocked 90° layer by around 870 MPa; two smaller cracks were also observed.

This progression is shown in Figure 16, where the black horizontal bar represents the onset and completion of crack development. As seen in Figure 16, the ability of both the modified and unmodified CFRE to resist cracking was reduced at cryogenic temperature, with the crack density traces initiating at lower applied stress values. The average stress at first crack for the unmodified CFRE was 116 ± 45.5 MPa [9], whereas the modified CFRE exhibited a 50% higher value of 174 ± 10.1 MPa. The lowest recorded stress at first crack was 53 MPa in an unmodified CFRE specimen, compared with 161 MPa in a modified CFRE specimen, an improvement of 204%. As indicated by the first data point on each crack density trace in Figure 16, the spread in first-crack stress was substantial for the unmodified CFRE, with a coefficient of variation of 39%, while the modified CFRE showed a much narrower range, with a coefficient of variation of 6%. Since the imaging system captured only 9 mm of the 115 mm gauge length, cracks forming outside the monitored region were not recorded. The wide scatter in the unmodified CFRE data therefore suggests that crack initiation may occur at lower applied stresses than directly observed, meaning that the improvement in the modified CFRE could be underestimated when using the average stress at first crack, particularly given the tight distribution and greater reliability of the modified system's mean value. While cracking behaviour at cryogenic temperature remained more brittle than at room temperature, the absence of pre-existing thermally induced microscale cracks and interfacial debonding from cool down, as illustrated by the cryo-SEM imaging in Section 3.3, appears to delay crack initiation under applied load in the modified CFRE. In contrast, the unmodified CFRE, which developed widespread matrix cracking and fibre–matrix debonding during cooling, exhibited lower and more variable first-crack stresses. This suggests that the suppression of thermally generated microscale damage prior to mechanical loading plays a critical role in improving crack resistance at cryogenic temperature under thermo-mechanical loading.

The matrix fracture results in Section 3.5 provide further context for this behaviour. Although crack initiation was delayed and higher stresses were reached before the first transverse crack formed during tensile testing of the modified CFRE, propagation at cryogenic temperature was rapid and unstable compared to the slower, more tortuous growth observed at room temperature. This shift does not indicate a reduction in measured fracture toughness, but rather

a reduction in the matrix's ability to deform at the crack tip as the fracture behaviour becomes increasingly matrix-dominated and the CSR toughening becomes less effective with decreasing temperature [48]. Consequently, energy dissipation mechanisms active at room temperature are reduced, and crack propagation becomes more abrupt despite the relatively stable measured fracture parameters. The improved cryogenic crack resistance of the modified CFRE therefore arises primarily from the suppression of thermally induced microscale damage before mechanical loading, as demonstrated in Section 3.3, rather than from greater resistance to crack propagation once cracking has initiated. While the modified matrix does not show the same apparent increase in cryogenic toughness observed in the unmodified epoxy, it resists microscale damage formation during cooling and maintains a relatively stable fracture response. This reduces the number of available crack-initiation sites and contributes to the improved performance under combined thermo-mechanical loading.

The internal pressure of tanks storing cryogenic propellants is commonly controlled at 0.2-0.3 MPa (2-3 bar) to ensure the fuel remains liquid [4, 59], significantly below the storage pressure of gaseous hydrogen tanks (350-700 bar [60]). To place the measured minimum stress at first transverse crack in context, a simple scaling exercise was carried out using LH_2 tank dimensions quoted by the UK's Aerospace Technology Institute FlyZero reports (2–5 m diameter) [61]. For a thin-walled, closed-end cylindrical tank the hoop stress is $\sigma_\theta = pr/t$, while for a thin-walled spherical tank the hoop stress is $\sigma_s = pr/(2t)$ [62], where p is internal pressure, r is vessel radius, and t is wall thickness. Using the FlyZero diameter range (r = 1-2.5 m) and the tested laminate thickness (t = 2.41 mm), the estimated stresses are: approximately 83–208 MPa for a cylindrical tank and 42–104 MPa for a spherical tank at 0.2 MPa pressure; and approximately 125–311 MPa for a cylindrical tank and 62–156 MPa for a spherical tank at 0.3 MPa pressure. The modified CFRE (minimum first-crack stress: 161 MPa at −155 °C) exceeds the estimated cylindrical vessel stress for several pressure–diameter combinations considered here and marginally exceeds the upper end of the spherical vessel stress range. In contrast, the unmodified CFRE (53 MPa at −155 °C) falls below the cylindrical range entirely and meets only the lowest-stress spherical configurations, reflecting a substantially diminished margin against transverse microcracking. It should be noted that this comparison is intended only as an order-

of-magnitude assessment and not a tank-design assessment. It does not account for factors such as (i) the lower LH_2 service temperature (~−253 °C), (ii) tank heads, bosses, openings and other geometric discontinuities, (iii) biaxial and multiaxial stress states and associated local stress concentrations, or (iv) laminate thickness, ply-angle and stacking-sequence optimisation for hoop-dominated tank loading rather than the cross-ply specimen behaviour considered here.

Conclusions

This study investigated the cryogenic damage resistance of a CSR, nanosilica and polysulphide-modified epoxy matrix CFRE, linking laminate-scale transverse cracking with hydrogen permeability, microscale damage formation, and matrix fracture response. The key findings and conclusions are as follows:

1. Compared to the unmodified CFRE, the modified CFRE showed substantially improved resistance to thermally induced transverse cracking under repeated cycling between −196 °C and +55 °C. No cracks were observed up to 100 cycles and the crack density after 250 cycles was 58% lower than in the unmodified CFRE.
2. The H_2 permeation data indicate that increased microcracking after thermal cycling increased hydrogen permeability mainly through higher diffusivity. The pressure–time curves showed a clear time lag followed by a linear steady-state region and xCT showed no through-thickness interconnected crack network, indicating diffusion-controlled transport rather than one dominated by leakage. Given the limited number of valid tests, these findings should be interpreted as a preliminary data trend rather than a statistically definitive comparison.
3. Cryo-SEM showed that matrix cracking and fibre–matrix debonding were suppressed in the modified CFRE during both rapid thermal shock and gradual cooling, despite its higher matrix CTE relative to the unmodified matrix. However, isolated fibre cracking and worsening of pre-existing fibre defects were still observed. This indicates that CTE mismatch alone does not control cryogenic damage initiation; strain accommodation within the matrix is also critical.

Journal Pre-proof

4. FIB-SEM showed that fibre damage formed during thermal cycling can remain confined to the exposed cross-section, but one examined fibre also contained a hairline crack extending into the interior. Although it cannot be determined whether this internal feature formed during thermal cycling or was pre-existing, its presence shows that fibre-scale damage associated with the observed surface features is not necessarily limited to the exposed cross-section. Local strain accumulation during cooling, fibre microstructural heterogeneity, or both, may therefore contribute to the observed fibre damage.
5. Under combined thermal and tensile loading at −155 °C, the modified CFRE increased the mean stress at first crack from 116 ± 45.5 MPa to 174 ± 10.1 MPa, and the minimum measured value from 53 MPa to 161 MPa. This improvement was attributed primarily to the suppression of thermally generated microscale damage during cooling, which reduced the number of available crack-initiation sites when tensile load was subsequently applied.
6. Matrix fracture testing showed that the modified epoxy maintained relatively stable K_{IC} and G_{IC} between +23 °C and −196 °C, but SEM fractography indicated reduced toughening activity at cryogenic temperature. This helps explain why crack propagation in the modified CFRE remained abrupt once initiated, even though first transverse crack initiation under tensile loading at −155 °C was delayed by the suppression of thermally induced microscale damage during cooling.

Overall, this work demonstrates a promising route for modifying CFRE matrices for LH_2 storage and shows that cryogenic microcracking resistance cannot be predicted from matrix fracture toughness or CTE mismatch alone. Matrix designs should therefore include low-temperature strain accommodation to prevent microscale matrix cracking and fibre–matrix debonding under cryogenic thermal loading. The preliminary fibre damage findings also warrant further investigation into carbon fibre damage during cryogenic thermal cycling and its implications for laminate performance.

Journal Pre-proof

Acknowledgements

This work was supported by the Engineering and Physical Sciences Research Council through the EPSRC Centre for Doctoral Training in Composites Science, Engineering and Manufacturing [grant number EP/S021728/1]. The authors thank James Hatcliffe and Jack Collins at NCC, as well as Judith Mantell of the Wolfson Bioimaging Facility, Max Bartlett at Composites Test and Evaluation and Dr. Dominic Palubiski at the Bristol Composites Institute. Funding was provided by the University of Bristol Science Partnership Office Exploratory Facilities Fund for work on the Plasma FIB, which was funded under the EPSRC Strategic Equipment fund, EP/W036576/1. The FEI Quanta 650 SEM and the Gatan *in-situ* cryo stage were supported by the Shell AIMS UTC and housed in the Harvey Flower EM suite at Imperial College London. SW acknowledges Imperial College London for funding his Imperial College Research Fellowship. Thanks are given to Dr. Stephan Sprenger and Dr. Peter Watkins from Evonik, Dr. Stefan Van Loy from Kaneka and Dr. Volker Burkhardt from Nouryon for supplying materials. The authors acknowledge the use of Dragonfly (Object Research Systems (ORS) Inc., Montreal, Canada) under a non-commercial academic licence.

CRediT author statement

James C. Griffith: Conceptualisation, Methodology, Investigation, Validation, Formal analysis, Visualisation, Data Curation, Writing - Original Draft. **Siyang Wang:** Methodology, Investigation, Visualisation, Writing - Review & Editing. **Christopher P. Jones:** Methodology, Investigation, Validation, Writing - Review & Editing. **Lui Skytree:** Resources, Methodology, Validation, Writing - Review & Editing. **Ricky Mazzeo:** Methodology, Investigation, Formal analysis, Writing - Review & Editing. **Cameron G. Woodgate:** Methodology, Visualisation, Writing - Review & Editing. **Huw Edwards:** Methodology, Writing – Review & Editing. **Karthik R. Ramakrishnan:** Writing - Review & Editing**,** Supervision. **Sébastien Rochat:** Writing - Review & Editing, Supervision. **Finn Giuliani:** Methodology, Resources, Writing - Review & Editing. **Marcus Walls-Bruck:** Resources, Writing - Review & Editing**,** Supervision. **Ian Hamerton:**

Conceptualisation, Methodology, Validation, Writing - Review & Editing, Supervision, Project administration, Funding acquisition.

Data availability

The data supporting the findings of this study are available from the corresponding author upon reasonable request.

References

1. Z. Sápi and R. Butler, *Properties of cryogenic and low temperature composite materials – A review.* Cryogenics, 2020. **111**: p. 103190.
2. R.R. Ratnakar, N. Gupta, K. Zhang, C. van Doorne, J. Fesmire, B. Dindoruk and V. Balakotaiah, *Hydrogen supply chain and challenges in large-scale LH2 storage and transportation.* International Journal of Hydrogen Energy, 2021. **46**(47): p. 24149-24168.
3. O. Barrera, D. Bombac, Y. Chen, T.D. Daff, E. Galindo-Nava, P. Gong, D. Haley, R. Horton, I. Katzarov, J.R. Kermode, C. Liverani, M. Stopher and F. Sweeney, *Understanding and mitigating hydrogen embrittlement of steels: a review of experimental, modelling and design progress from atomistic to continuum.* Journal of Materials Science, 2018. **53**(9): p. 6251-6290.
4. N. Liu, B. Ma, F. Liu, W. Huang, B. Xu, L. Qu and Y. Yang, *Progress in research on composite cryogenic propellant tank for large aerospace vehicles.* Composites Part A: Applied Science and Manufacturing, 2021. **143**: p. 106297.
5. Ł. Figiel, M.G. De Angelis, F. Janssen, D. Vehlow, S. Giannis, L. Skytree, M. Walls-Bruck and A. Douglas, *Polymers and composites for hydrogen economy: a perspective.* Journal of Materials Science: Composites, 2025. **6**(1): p. 11.
6. J. Hohe, A. Neubrand, S. Fliegener, C. Beckmann, M. Schober, K.-P. Weiss and S. Appel, *Performance of fiber reinforced materials under cryogenic conditions—A review.* Composites Part A: Applied Science and Manufacturing, 2021. **141**: p. 106226.
7. J. Srisuriyachot, W. Singhapong, P. Rodriguez Santana, C.M. Sangan, C. Bowen, I.P. Dolbnya, R. Butler and A.J.G. Lunt, *Quantification of the thermal expansion of carbon fibres in CFRP at low temperatures using X-ray diffraction.* Composites Part B: Engineering, 2025. **305**: p. 112697.
8. Z. Ran, Y. Yan, J. Li, Z. Qi and L. Yang, *Determination of thermal expansion coefficients for unidirectional fiber-reinforced composites.* Chinese Journal of Aeronautics, 2014. **27**(5): p. 1180-1187.
9. J.C. Griffith, S. Wang, D.R. Palubiski, K.R. Ramakrishnan, S. Rochat, F. Giuliani, M. Walls-Bruck and I. Hamerton, *Investigating the microcracking behaviour of a commercial epoxy matrix under cryogenic conditions.* Composites Part A: Applied Science and Manufacturing, 2025. **199**: p. 109190.
10. H. Edwards, R. Clark, D. Galpin, M. Walls-Bruck, B.C. Kim and J.M. Dulieu-Barton. *Characterising composite microcracking behaviour under load at cryogenic temperature*. in *21st European Conference on Composite Materials (ECCM21)*. 2024. Nantes, France.
11. H. Edwards, D. Galpin, M. Walls-Bruck, B.C. Kim and J.M. Dulieu-Barton. *In-situ observation of microcrack formation in carbon fibre reinforced composites under mechanical load at cryogenic temperatures*. in *Cryogenic Engineering Conference and International Cryogenic Materials Conference*. 2023. Honolulu, Hawaii.

12. K. Fujishiro, T. Ogasawara, K. Mizutani, H. Kumazawa and T. Aoki, *Microscopic damage behavior in CFRP cross-ply laminates at cryogenic temperature.* Composites Science and Technology, 2024. **256**: p. 110774.
13. Y.-f. Su, S.-n. Wang, L.-h. Ma, H. Gao, H.-s. Lei and W. Zhou, *Cryogenic damage mechanism of CFRP laminates under bending load via in-situ fiber-optic acoustic emission and mode decomposition.* Composites Part B: Engineering, 2026. **308**: p. 112994.
14. Y.-f. Su, T.-y. Zhang, H. Sun, L.-h. Ma and W. Zhou, *Cryogenic damage behavior of carbon fiber reinforced polymer composite laminates via fiber-optic acoustic emission.* Composites Part A: Applied Science and Manufacturing, 2024. **186**: p. 108435.
15. L. Ma, X. Du, W. Zhou, C. Huang, W. Sun and B. Wang, *Acoustic emission and multiscale computation-guided tensile damage identification in woven composite laminates at cryogenic temperatures as low as 20 K.* Thin-Walled Structures, 2024. **205**: p. 112464.
16. Y. Li, J. Meng, G. Niu, H. Yang, P. Wang, H. Lei and D. Fang, *Cryogenic damage mechanisms of CFRP laminates based on in-situ X-ray computed tomography characterization.* Composites Science and Technology, 2024. **247**: p. 110413.
17. Y. Li, Y. Wei, J. Meng, L. Zhang, P. Wang, H. Zheng and H. Lei, *Damage evolution characterization of glass fabric composites at cryogenic temperatures via in-situ tensile X-ray computed tomography tests.* Composites Communications, 2022. **35**: p. 101326.
18. K. Rivers, J. Sikora and S. Sankaran, *Detection of micro-leaks through complex geometries under mechanical load and at cryogenic temperature*, in *19th AIAA Applied Aerodynamics Conference*. 2001.
19. V.T. Bechel, M. Negilski and J. James, *Limiting the permeability of composites for cryogenic applications.* Composites Science and Technology, 2006. **66**(13): p. 2284-2295.
20. S. Choi and B.V. Sankar, *Gas permeability of various graphite/epoxy composite laminates for cryogenic storage systems.* Composites Part B: Engineering, 2008. **39**(5): p. 782-791.
21. M. Flanagan, D.M. Grogan, J. Goggins, S. Appel, K. Doyle, S.B. Leen and C.M. Ó Brádaigh, *Permeability of carbon fibre PEEK composites for cryogenic storage tanks of future space launchers.* Composites Part A: Applied Science and Manufacturing, 2017. **101**: p. 173-184.
22. S. Saha, R.W. Sullivan and M.L. Baker, *Gas permeability of three-dimensional stitched carbon/epoxy composites for cryogenic applications.* Composites Part B: Engineering, 2021. **216**: p. 108847.
23. S. Saha, R.W. Sullivan and M.L. Baker, *Gas permeability mitigation of cryogenically cycled stitched composites using thin plies.* Composite Structures, 2023. **304**: p. 116352.
24. J. Koord, H. Kumazawa, A. Fischer, T. Ebina, O. Völkerink and C. Hühne, *Investigation of permeability and leakage in composite materials for application in cryogenic storage systems.* Composites Part B: Engineering, 2026. **316**: p. 113580.
25. D. Schultheiß, *Permeation barrier for lightweight liquid hydrogen tanks*, in *Augsburg Univ. (Germany). Mathematisch-Naturwissenschaftliche Fakultaet*. 2007: Germany.
26. E. Stokes. *Hydrogen permeability of polymer-based composites under bi-axial strain and cryogenic temperatures*. in *45th AIAA/ASME/ASCE/AHS/ASC Structures, Structural Dynamics & Materials Conference.* 2004.
27. R. Grenoble and T. Gates. *Hydrogen gas leak rate testing and post-testing assessment of microcrack damaged composite laminates*. in *47th AIAA/ASME/ASCE/AHS/ASC Structures, Structural Dynamics, and Materials Conference*. 2006.
28. J. Humpenöder, *Gas permeation of fibre reinforced plastics.* Cryogenics, 1998. **38**(1): p. 143-147.
29. M.S. Islam, L.F. Benninger, G. Pearce and C.-H. Wang, *Toughening carbon fibre composites at cryogenic temperatures using low-thermal expansion nanoparticles.* Composites Part A: Applied Science and Manufacturing, 2021. **150**: p. 106613.
30. M.S. Islam, W. Chang, Z. Sha, J. Wang, S. Wu, L.R.F. Rose, A.J. Kinloch and C.H. Wang, *Mitigating cryogenic microcracking in carbon-fibre reinforced polymer*

composites using negative thermal-expansion nanoparticles functionalized by a polydopamine coating. Composites Part B: Engineering, 2023. **257**: p. 110676.
31. J. Wang, W. Chang, M.S. Islam, F. Huang, S. Wu, L.R.F. Rose, J. Zhang and C.H. Wang, *Toughening epoxy by nano-structured block copolymer to mitigate matrix microcracking of carbon fibre composites at cryogenic temperatures.* Composites Science and Technology, 2024. **251**: p. 110548.
32. C.-B. Qu, T. Wu, G.-W. Huang, N. Li, M. Li, J.-L. Ma, Y. Liu and H.-M. Xiao, *Improving cryogenic mechanical properties of carbon fiber reinforced composites based on epoxy resin toughened by hydroxyl-terminated polyurethane.* Composites Part B: Engineering, 2021. **210**: p. 108569.
33. Y. He, Q. Chen, S. Yang, C. Lu, M. Feng, Y. Jiang, G. Cao, J. Zhang and C. Liu, *Micro-crack behavior of carbon fiber reinforced Fe3O4/graphene oxide modified epoxy composites for cryogenic application.* Composites Part A: Applied Science and Manufacturing, 2018. **108**: p. 12-22.
34. Y. He, Q. Li, T. Kuila, N.H. Kim, T. Jiang, K. Lau and J.H. Lee, *Micro-crack behavior of carbon fiber reinforced thermoplastic modified epoxy composites for cryogenic applications.* Composites Part B: Engineering, 2013. **44**(1): p. 533-539.
35. M. Nobelen, B.S. Hayes and J.C. Seferis, *Cryogenic microcracking of rubber toughened composites.* Polymer Composites, 2003. **24**(6): p. 723-730.
36. M. Nobelen, B.S. Hayes and J.C. Seferis, *Influence of elastomer distribution on the cryogenic microcracking of carbon fiber/epoxy composites.* Journal of Applied Polymer Science, 2003. **90**(8): p. 2268-2275.
37. J.F. Timmerman, B.S. Hayes and J.C. Seferis, *Nanoclay reinforcement effects on the cryogenic microcracking of carbon fiber/epoxy composites.* Composites Science and Technology, 2002. **62**(9): p. 1249-1258.
38. J.C. Griffith, S. Rajeshirke, K.R. Ramakrishnan, S. Rochat, M. Walls-Bruck and I. Hamerton, *A multifunctional epoxy matrix for cryogenic microcrack resistance via core-shell rubber, nanosilica and disulphide-based modification.* Manuscript under review, 2026.
39. V.T. Bechel and R.Y. Kim, *Damage trends in cryogenically cycled carbon/polymer composites.* Composites Science and Technology, 2004. **64**(12): p. 1773-1784.
40. S. Saha and R.W. Sullivan. *Gas permeability of 3D printed thermoplastic composites for cryogenic applications*. in *Proceedings of the American Society for Composites thirty-seventh technical conference*. 2022.
41. J.A. Nairn, *Matrix microcracking in composites*, in *Polymer Matrix Composites*. 2001, Elsevier Science.
42. M. Wadsworth, *Tooling fundamentals for resin transfer moulding*, in *Resin Transfer Moulding for Aerospace Structures*, T.M. Kruckenberg and R. Paton, Editors. 1998, Springer Netherlands: Dordrecht. p. 282-337.
43. *ISO 15105-1:2007 Plastics — Film and sheeting — Determination of gas-transmission rate — Part 1: Differential-pressure methods*. 2007, International Organization for Standardisation: Geneva.
44. *ASTM D5045-14 (Reapproved 2022) Standard test methods for plane-strain fracture toughness and strain energy release rate of plastic materials*. 2022, ASTM International.
45. S. Saha and R.W. Sullivan, *A review on gas permeability of polymer matrix composites for cryogenic applications.* Journal of Composite Materials, 2024. **58**(6): p. 827-847.
46. A.T. Rhead, S. Hua and R. Butler, *Damage resistance and damage tolerance of hybrid carbon-glass laminates.* Composites Part A: Applied Science and Manufacturing, 2015. **76**: p. 224-232.
47. M.C. Lafarie-Frenot and S. Rouquie, *Influence of oxidative environments on damage in c/epoxy laminates subjected to thermal cycling.* Composites Science and Technology, 2004. **64**(10): p. 1725-1735.
48. J.C. Griffith, A. Stöger, M. Bartlett, K.R. Ramakrishnan, S. Rochat, M. Walls-Bruck and I. Hamerton, *Fracture toughness of core-shell rubber modified epoxies at low and cryogenic temperatures: Evaluating the influence of the glass transition temperature of the rubber core.* Reactive and Functional Polymers, 2026. **225**: p. 106789.
49. L.A. Giannuzzi and F.A. Stevie, *Introduction to focused ion beams: Instrumentation, theory, techniques, and practice*. 2005, New York: Springer.

50. D. Kim, S. Lee, W. Hong, H. Lee, S. Jeon, S. Han and J. Nam, *Image segmentation for FIB-SEM serial sectioning of a Si/C-graphite composite anode microstructure based on preprocessing and global thresholding.* Microscopy and Microanalysis, 2019. **25**(5): p. 1139-1154.
51. I.A. Rashkovan and Y.G. Korabel'nikov, *The effect of fiber surface treatment on its strength and adhesion to the matrix.* Composites Science and Technology, 1997. **57**(8): p. 1017-1022.
52. H. Zhang, Z. Zhang and C. Breidt, *Comparison of short carbon fibre surface treatments on epoxy composites: I. Enhancement of the mechanical properties.* Composites Science and Technology, 2004. **64**(13): p. 2021-2029.
53. S. Nishijima, Y. Honda and T. Okada, *Application of the positron annihilation method for evaluation of organic materials for cryogenic use.* Cryogenics, 1995. **35**(11): p. 779-781.
54. M. Yan, Y. Liu, W. Jiang, W. Qin, Y. Yan, L. Wan, W. Jiao and R. Wang, *Mechanism of matrix influencing the cryogenic mechanical property of carbon fibre reinforced epoxy resin composite.* Composites Communications, 2022. **33**: p. 101220.
55. Y. Zhao, Z.-K. Chen, Y. Liu, H.-M. Xiao, Q.-P. Feng and S.-Y. Fu, *Simultaneously enhanced cryogenic tensile strength and fracture toughness of epoxy resins by carboxylic nitrile-butadiene nano-rubber.* Composites Part A: Applied Science and Manufacturing, 2013. **55**: p. 178-187.
56. A.C. Garg and Y.-W. Mai, *Failure mechanisms in toughened epoxy resins—A review.* Composites Science and Technology, 1988. **31**(3): p. 179-223.
57. A.J. Kinloch, S.J. Shaw, D.A. Tod and D.L. Hunston, *Deformation and fracture behaviour of a rubber-toughened epoxy: 1. Microstructure and fracture studies.* Polymer, 1983. **24**(10): p. 1341-1354.
58. C. Yan, K. Xiao, L. Ye and Y.-W. Mai, *Numerical and experimental studies on the fracture behavior of rubber-toughened epoxy in bulk specimen and laminated composites.* Journal of Materials Science, 2002. **37**(5): p. 921-927.
59. G. Abumeri, D. Kosareo and J. Roche, *Cryogenic composite tank design for next generation launch technology*, in *40th AIAA/ASME/SAE/ASEE Joint Propulsion Conference and Exhibit*. 2004.
60. J.D. Worth, J.C. Griffith, V.P. Ting and C.F.J. Faul, *Enhancing hydrogen storage through processable porous composite membranes.* International Journal of Hydrogen Energy, 2025. **193**: p. 152427.
61. E. Aygin, N. Town, E. Burrows, L. Hadnum, M. Whillier and K. Milne, *FZO-IST-POS-0037: Advanced Manufacturing*. 2022, FlyZero, Aerospace Technology Institute.
62. G.B. Sinclair and J.E. Helms, *A review of simple formulae for elastic hoop stresses in cylindrical and spherical pressure vessels: What can be used when.* International Journal of Pressure Vessels and Piping, 2015. **128**: p. 1-7.

Journal Pre-proof

- The modified CFRE prevented cracking up to 100 thermal cycles and reduced crack density by 58% after 250 cycles.
- H_2 permeation increased after 250 thermal cycles, with xCT showing no through-thickness leakage path.
- *In-situ* cryo-SEM showed suppressed matrix cracking and fibre–matrix debonding.
- Minimum recorded stress at first crack increased by 204% at −155 °C in the modified CFRE.
- Cryogenic microcrack resistance depended on suppressing microscale damage initiation, rather than matrix toughness or CTE mismatch alone.

Journal Pre-proof

Journal Pre-proof

Declaration of interests

☐ The authors declare that they have no known competing financial interests or personal relationships that could have appeared to influence the work reported in this paper.

☒ The authors declare the following financial interests/personal relationships which may be considered as potential competing interests:

J.C. Griffith, K.R. Ramakrishnan, S. Rochat, M. Walls-Bruck and I. Hamerton are named inventors on a pending patent application assigned to the University of Bristol. The remaining authors declare that they have no known competing financial interests or personal relationships that could have appeared to influence the work reported in this paper.

Journal Pre-proof